

Dry double-sided tape for adhesion of wet tissues and devices

<https://doi.org/10.1038/s41586-019-1710-5>

Received: 17 September 2018

Accepted: 20 August 2019

Published online: 30 October 2019

Hyunwoo Yuk^{1,8}, Claudia E. Varela^{2,3,8}, Christoph S. Nabzdyk^{4,5}, Xinyu Mao¹, Robert F. Padera⁶, Ellen T. Roche^{1,2,3} & Xuanhe Zhao^{1,7*}

Two dry surfaces can instantly adhere upon contact with each other through intermolecular forces such as hydrogen bonds, electrostatic interactions and van der Waals interactions^{1,2}. However, such instant adhesion is challenging when wet surfaces such as body tissues are involved, because water separates the molecules of the two surfaces, preventing interactions^{3,4}. Although tissue adhesives have potential advantages over suturing or stapling^{5,6}, existing liquid or hydrogel tissue adhesives suffer from several limitations: weak bonding, low biological compatibility, poor mechanical match with tissues, and slow adhesion formation^{5–13}. Here we propose an alternative tissue adhesive in the form of a dry double-sided tape (DST) made from a combination of a biopolymer (gelatin or chitosan) and crosslinked poly(acrylic acid) grafted with *N*-hydrosuccinimide ester. The adhesion mechanism of this DST relies on the removal of interfacial water from the tissue surface, resulting in fast temporary crosslinking to the surface. Subsequent covalent crosslinking with amine groups on the tissue surface further improves the adhesion stability and strength of the DST. In vitro mouse, in vivo rat and ex vivo porcine models show that the DST can achieve strong adhesion between diverse wet dynamic tissues and engineering solids within five seconds. The DST may be useful as a tissue adhesive and sealant, and in adhering wearable and implantable devices to wet tissues.

Existing tissue adhesives—which are in the form of liquids or wet hydrogels—mostly rely on the diffusion of their molecules (for example, monomers, macromers or polymers) through the interfacial water to form bonds with the polymer networks of tissues^{5–12} (Fig. 1a, b). By contrast, animals capable of forming adhesion in wet environments commonly possess mechanisms (for example, mussel, barnacle and spider-web glues) to remove interfacial water from the contact surfaces in order to form bonds^{14–16}. Inspired by these examples in nature, we have engineered our DST to adopt a dry-crosslinking mechanism to remove interfacial water and form adhesion on wet tissues (Fig. 1c, d and Extended Data Fig. 1).

The DST consists of two major components: first, poly(acrylic acid) grafted with *N*-hydroxysuccinimide ester (PAAc-NHS ester) crosslinked by biodegradable gelatin methacrylate; and second, biodegradable biopolymers (for example, gelatin or chitosan). The negatively charged carboxylic acid groups in the PAAc-NHS ester facilitate the quick hydration and swelling of the DST to dry the wet surfaces of various tissues under gentle pressure of around 1 kPa, applied for less than 5 seconds. (See Supplementary Information for a quantitative model showing how the DST dries interfacial water, and Supplementary Figs. 1–6.) Simultaneously, the carboxylic acid groups in the PAAc-NHS ester form intermolecular bonds (for example, hydrogen bonds and electrostatic interactions) with the tissue surfaces (Fig. 1d and Extended Data

Fig. 1). To provide stable adhesion, the NHS ester groups grafted on the PAAc also couple covalently with primary amine groups on various tissues within a few minutes, without the need for further pressure (Extended Data Figs. 1, 2). After adhering onto tissues, the swollen DST becomes a thin hydrogel layer with an equilibrium water content of around 92% by volume (Extended Data Fig. 3). Because the swollen DST integrates mechanisms for high stretchability and mechanical dissipation^{17,18}, it exhibits a high fracture toughness of more than 1,000 J m^{−2} (Supplementary Figs. 7, 8), which is crucial in achieving tough adhesion of the swollen DST^{19,20}.

The dry DST takes the form of a conformable thin film that can be applied on non-planar tissue surfaces (Extended Data Fig. 4). It can be fabricated into diverse shapes such as flat sheets, perforated sheets and adhesive-tape-like rolls (Fig. 1e). The DST, in its fully swollen state, exhibits a shear modulus of 2.5–5 kPa and the ability to stretch to more than 16 times the original length, capable of mechanically matching soft tissues²¹ (Fig. 1f, g). To remove potentially cytotoxic residual reagents, we thoroughly purified the DST during its preparation (Extended Data Fig. 5). The in vitro biocompatibility of the DST-conditioned medium is comparable to that of the control medium, showing no observable decrease in the in vitro viability of mouse embryonic fibroblasts (MEFs) after 24-h culture (Fig. 1h). The crosslinkers (that is, gelatin methacrylate) for PAAc-NHS ester and the biopolymers (that is, gelatin

¹Department of Mechanical Engineering, Massachusetts Institute of Technology, Cambridge, MA, USA. ²Institute for Medical Engineering and Science, Massachusetts Institute of Technology, Cambridge, MA, USA. ³Harvard-MIT Program in Health Sciences and Technology, Cambridge, MA, USA. ⁴Department of Anesthesiology and Perioperative Medicine, Mayo Clinic, Rochester, MN, USA. ⁵Department of Anesthesia, Critical Care and Pain Medicine, Massachusetts General Hospital, Harvard Medical School, Boston, MA, USA. ⁶Department of Pathology, Brigham and Women's Hospital, Harvard Medical School, Boston, MA, USA. ⁷Department of Civil and Environmental Engineering, Massachusetts Institute of Technology, Cambridge, MA, USA. ⁸These authors contributed equally: Hyunwoo Yuk, Claudia E. Varela. *e-mail: zhaox@mit.edu

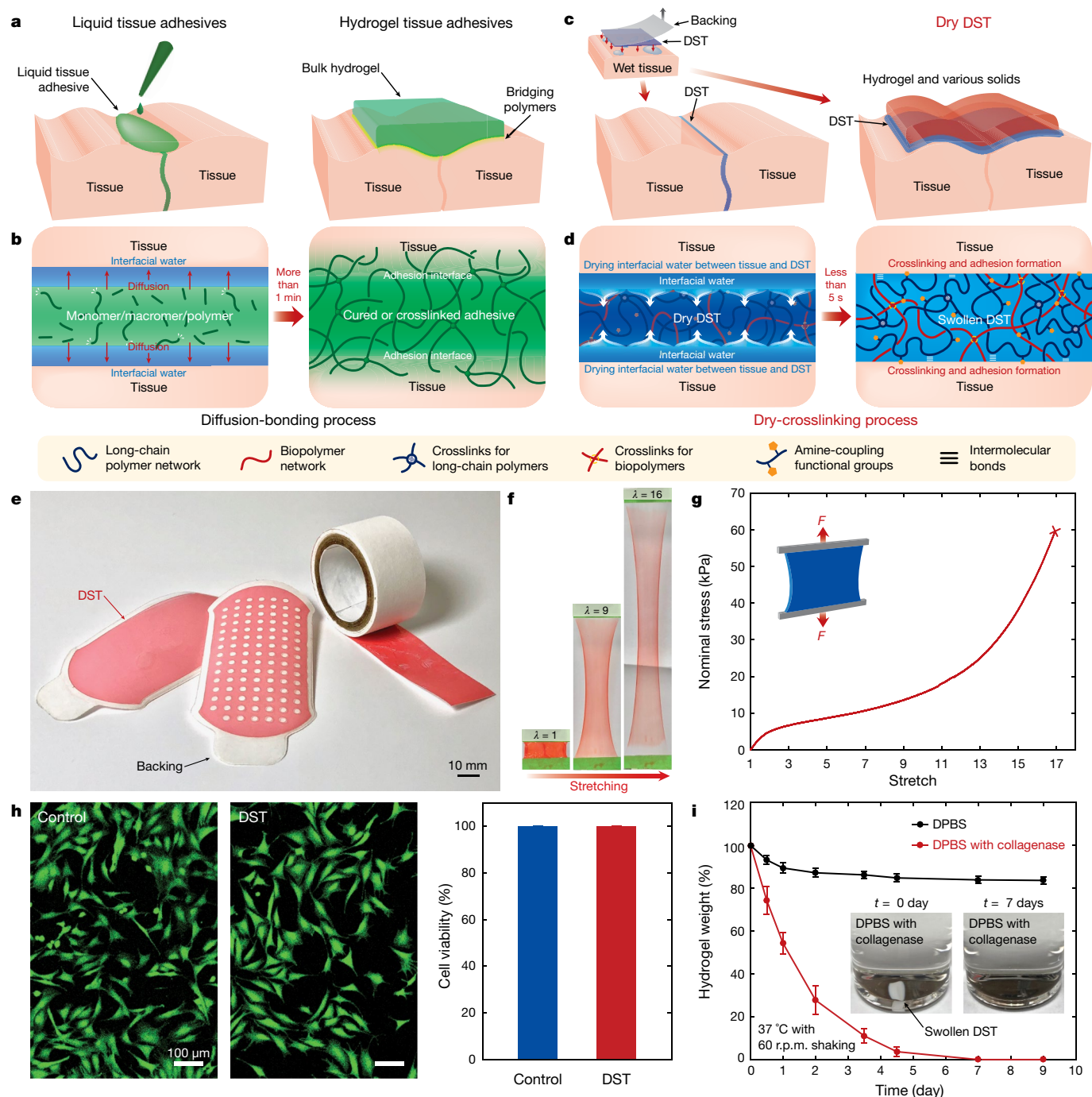


Fig. 1 | Dry DST and dry-crosslinking mechanism for adhesion of wet tissues and devices. **a**, Existing tissue adhesives take the form of liquids or wet hydrogels. **b**, Adhesion formation by these existing adhesives mostly relies on the diffusion of monomers, macromers or polymers towards the tissues. **c**, Our proposed tissue adhesive takes the form of a dry DST. **d**, The dry-crosslinking mechanism for the DST integrates the drying of interfacial water by hydration and swelling of the dry DST, temporary crosslinking, and covalent crosslinking (the latter involving the formation of covalent bonds between the DST and amine groups on tissues). **e**, The DST can take on various shapes owing to its

high flexibility in fabrication. The DST is coloured with a red food dye for visualization. **f, g**, Photographs (**f**) and nominal stress versus stretch curve (**g**) for the DST in its swollen state, stretched to more than 16 times the original length. The DST is coloured with a red food dye for visualization. λ , stretch; F , force. **h**, In vitro biocompatibility of the DST in a live/dead assay of mouse embryonic fibroblasts (MEFs) after 24 hours of culture. **i**, In vitro biodegradation of the gelatin-based DST in Dulbecco's phosphate-buffered saline (DPBS) with or without collagenase. Values in panels **h, i** represent the mean and the standard deviation ($n = 3-5$).

or chitosan) in the DST are biodegradable by endogenous enzymes (for example, collagenase, lysozyme or *N*-acetyl- β -D-glucosaminidase (NAGase)) at varying rates. For example, gelatin typically degrades more quickly than chitosan under physiological conditions²². Hence, the in vitro biodegradation rate of the DST can be controlled over time periods from a week (for the gelatin-based DST) to several months

(for the chitosan-based DST) by tuning its composition (Fig. 1i and Supplementary Fig. 9).

To evaluate the adhesion performance of the DST, we conduct three different types of mechanical tests, measuring the interfacial toughness by peel tests, the shear strength by lap-shear tests and the tensile strength by tensile tests (according to the following testing standards

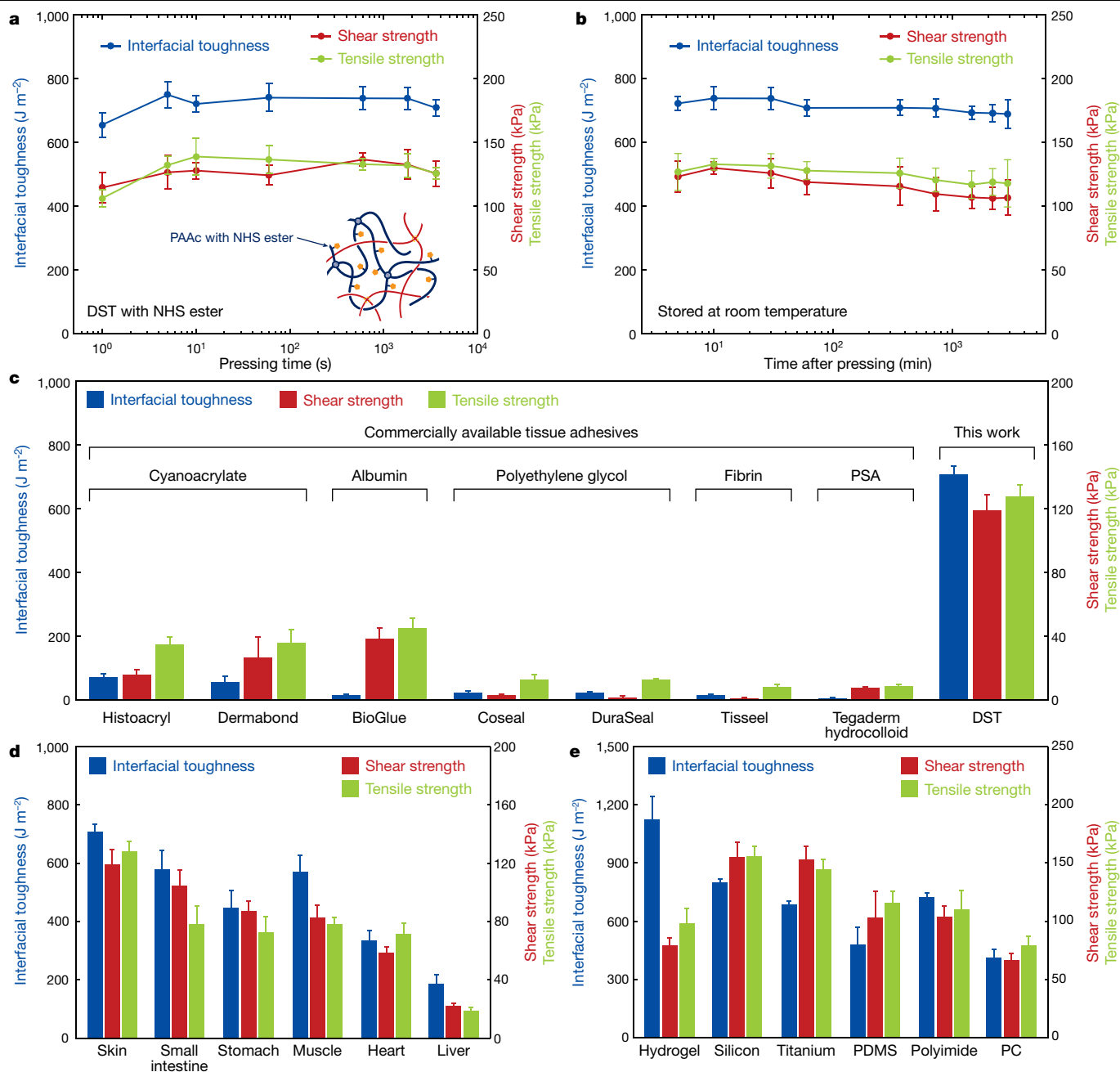


Fig. 2 | Adhesion performance of the DST. **a**, Interfacial toughness and shear and tensile strength versus pressing time for wet porcine skins adhered using the DST with NHS ester. **b**, Interfacial toughness and shear and tensile strength versus time after pressing for wet porcine skins adhered using the DST with NHS ester. **c**, Comparison of adhesion performances of the DST and various

commercially available tissue adhesives. PSA, pressure-sensitive adhesives.

d, Interfacial toughness and shear and tensile strength between various tissues adhered by the DST. **e**, Interfacial toughness and shear and tensile strength between porcine skin and various engineering solids adhered by the DST. Values represent the mean and standard deviation ($n = 3-5$).

for tissue adhesives: ASTM F2256 for 180-degree peel tests, ASTM F2255 for lap-shear tests, and ASTM F2258 for tensile tests; Extended Data Fig. 6 and Supplementary Fig. 10). We first choose wet porcine skin as the model tissue for evaluation of adhesion performance, owing to its mechanical robustness and close resemblance to human skin¹². The DST can establish tough (with an interfacial toughness of more than 710 J m^{-2}) and strong (with a shear and tensile strength of more than 120 kPa) adhesion between wet porcine skins upon contact and application of gentle pressure (1 kPa) for less than 5 seconds (Fig. 2a, Supplementary Fig. 11 and Supplementary Video 1). The tissues adhered by the DST exhibit a relatively small decrease (of less than 10%) in the measured interfacial toughness and strength more than 48 h after the initial pressing (Fig. 2b). Furthermore, the DST can maintain its ability

to form robust adhesion on wet tissues after being stored for more than 2 weeks (Supplementary Fig. 12).

We also examine the importance of covalent crosslinking after intermolecular crosslinking on the adhesion performance of the DST. We test the adhesion performance of the DST without grafted NHS ester on the PAAc, which cannot form covalent crosslinks with tissues (Extended Data Fig. 7). Although the DST without NHS ester can provide tough (with an interfacial toughness greater than 500 J m^{-2}) and strong (with a shear and tensile strength more than 80 kPa) adhesion upon application between wet porcine skins (Extended Data Fig. 7a), the adhesion performance shows substantial deterioration over time (Extended Data Fig. 7b), owing to the unstable and temporary nature of the intermolecular bonds in wet environments³. Hence, both the

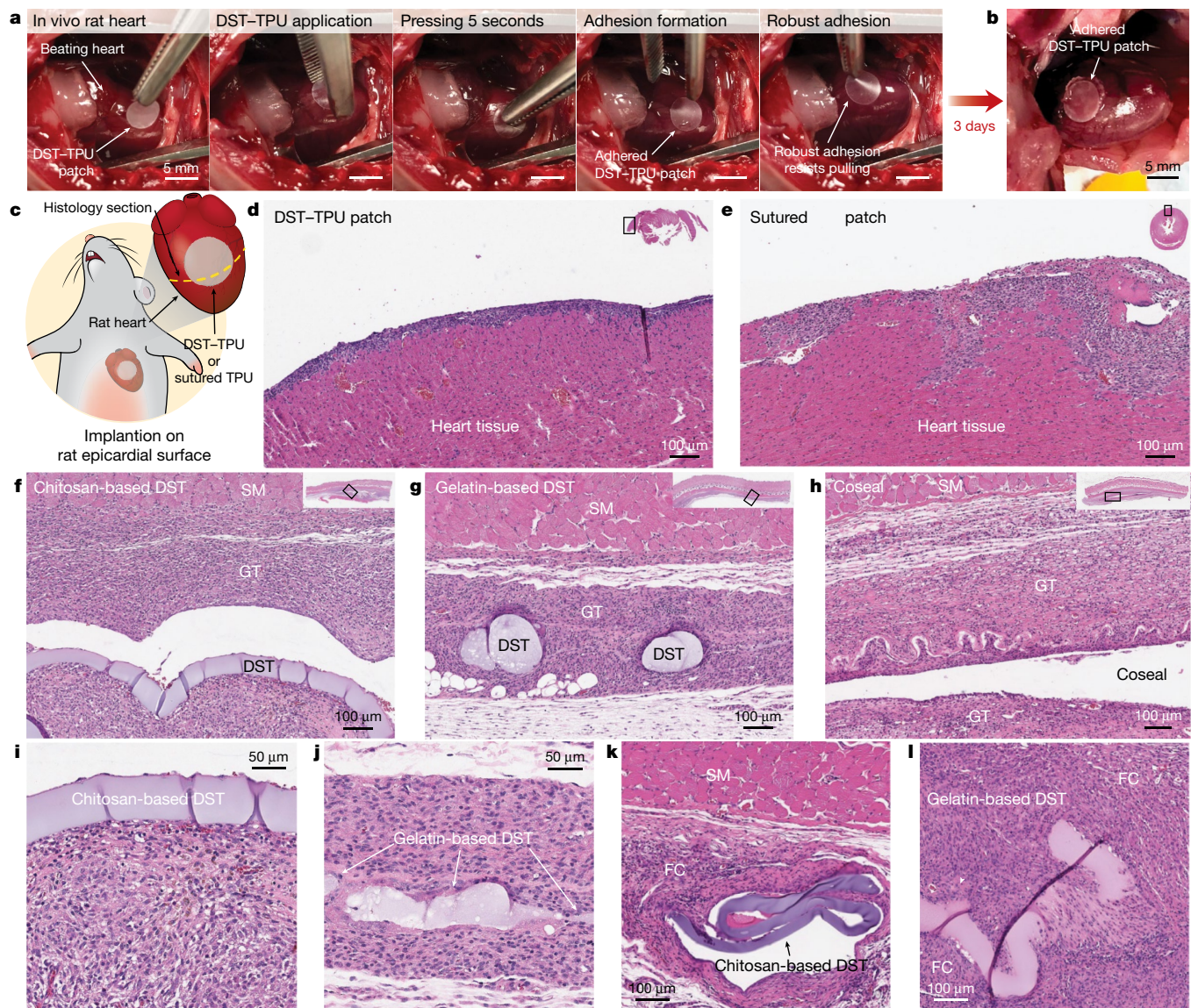


Fig. 3 | In vivo adhesion, biocompatibility, and biodegradability of the DST.

a, Adhesion of a DST-TPU hybrid patch on a beating rat heart in vivo. **b**, The DST-TPU patch adhered on the rat heart 3 days after implantation in vivo. **c**, A schematic illustration of the section taken for histology (dotted yellow line) through a DST-TPU or a sutured TPU patch implanted on the rat epicardial surface. **d**, **e**, Representative histological images of the DST-TPU patch (**d**) and the sutured TPU patch (**e**) stained with haematoxylin and eosin (H&E). **f**–**h**, Representative histological images of the chitosan-based DST (**f**), the

gelatin-based DST (**g**) and the Coseal (**h**), stained with H&E. **i**, **j**, Representative histological images stained with H&E for assessment of the biodegradation of subcutaneously implanted chitosan-based DST (**i**) and gelatin-based DST (**j**) after 2 weeks. **k**, **l**, Representative histological images stained with H&E for assessment of the biocompatibility and biodegradation of subcutaneously implanted chitosan-based DST (**k**) and gelatin-based DST (**l**) after 4 weeks. SM, GT and FC indicate skeletal muscle, granulation tissue and fibrous capsule, respectively. All experiments were repeated three or four times with similar results.

temporary crosslinks and the subsequent covalent crosslinks are necessary for stable and robust adhesion of wet surfaces, supporting our proposed mechanism (Fig. 1d and Extended Data Fig. 1).

We further test the adhesion performance of the DST under cyclic loading conditions. Two porcine heart tissues adhered by the DST maintain a high interfacial toughness of more than 650 J m^{-2} during cyclic loading over 5,000 cycles with physiologically relevant strain (30% tensile strain) (Supplementary Fig. 13). In addition, the DST can provide similarly high interfacial toughness (of more than 640 J m^{-2}) and shear and tensile strength (of more than 85 kPa) on blood-covered porcine tissues after washout with saline²³ (Supplementary Fig. 14).

The DST demonstrates superior adhesion performance compared with existing tissue adhesives, including commercially available cyanoacrylate adhesives (Histoacryl and Dermabond), albumin-based adhesives (BioGlue), polyethylene-glycol-based adhesives (Coseal and

DuraSeal), fibrin glues (Tisseel), hydrophilic pressure-sensitive adhesives (Tegaderm hydrocolloid), as well as nanoparticle solutions⁸ and ultraviolet-curable surgical glues²⁴ (Fig. 2c and Extended Data Fig. 8). We find that these existing tissue adhesives require a relatively long time to form adhesion (longer than 1 min; Extended Data Fig. 8) and exhibit limited adhesion performance on wet tissues (with an interfacial toughness of less than 20 J m^{-2} and a shear and tensile strength of less than 45 kPa; Fig. 2c), consistent with published performances⁷. The DST provides a higher interfacial toughness (up to $1,150 \text{ J m}^{-2}$) and shear and tensile strength (up to 160 kPa) than existing tissue adhesives, and forms the adhesion in less than 5 seconds (Fig. 2c–e and Extended Data Fig. 8). Although tough hydrogel adhesives can achieve a similarly high interfacial toughness of more than $1,000 \text{ J m}^{-2}$ on wet tissues, they require steady pressure application for substantially longer periods of time (5–30 min) on tissue surfaces to form the adhesion^{12,25}.

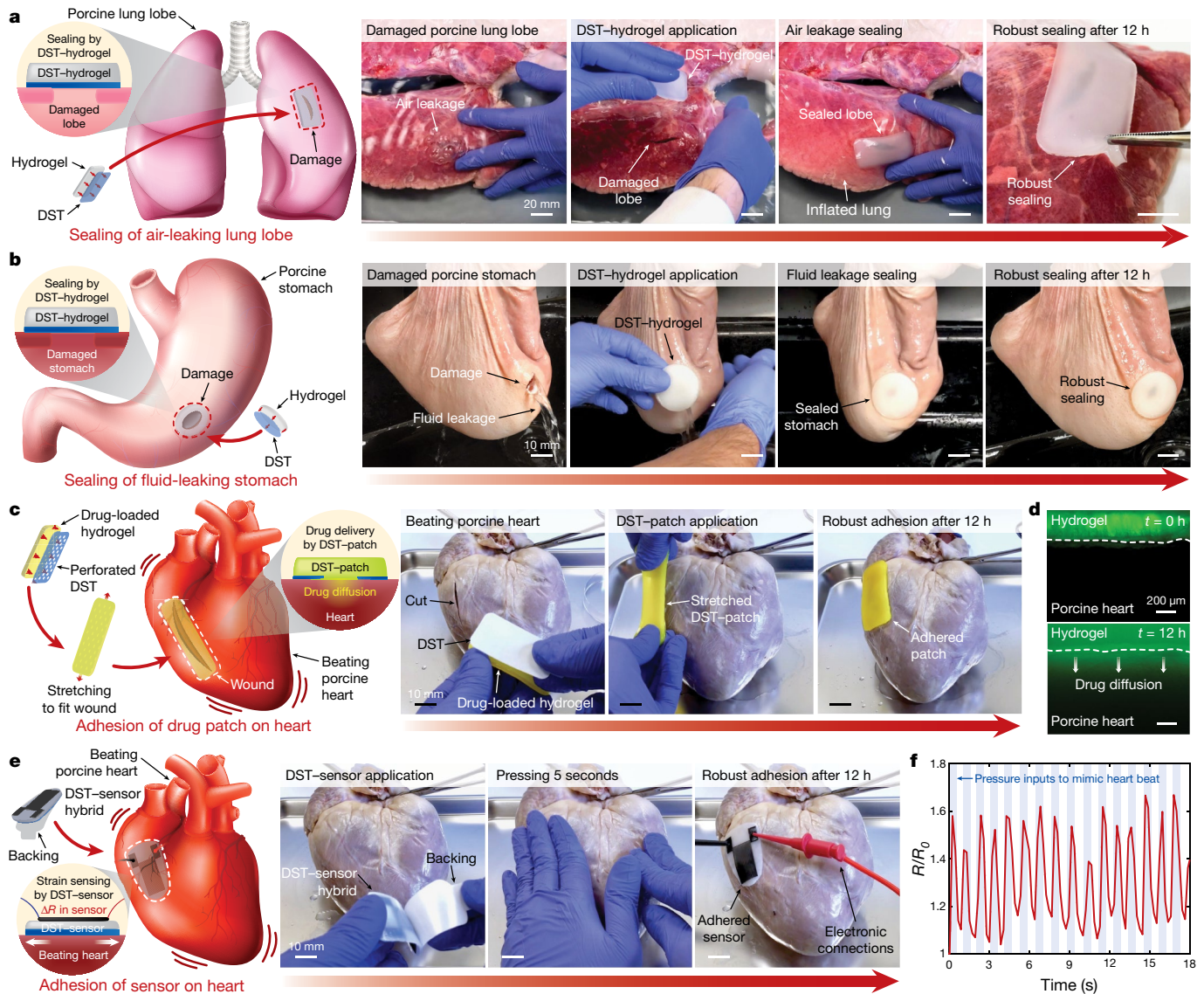


Fig. 4 | Potential applications of the DST. **a**, Sealing of an air-leaking lacerated ex vivo porcine lung lobe by a hydrogel patch adhered with the DST. **b**, Sealing of a fluid-leaking ex vivo porcine stomach by a hydrogel patch adhered with the DST. **c**, DST-mediated adhesion of a drug-loaded patch on a beating ex vivo porcine heart with a cut. **d**, Diffusion of a mock drug (fluorescein) from a DST-adhered drug patch into the ex vivo porcine heart tissue over time. **e**, Adhesion

of a DST-strain-sensor hybrid on a beating ex vivo porcine heart. **f**, Normalized electrical resistance (R/R_0) of the DST-adhered strain sensor over time, in order to measure deformation of the beating heart. The blue shades in the graph indicate the intervals during which pressure inputs are introduced to the ex vivo porcine heart to mimic beating.

The DST can be applied to various wet tissues, including skin, small intestine, stomach, muscle, heart and liver (Fig. 2d and Supplementary Video 2), with high interfacial toughness (more than 710 J m^{-2} for skin, 580 J m^{-2} for small intestine, 450 J m^{-2} for stomach, 570 J m^{-2} for muscle, 340 J m^{-2} for heart and 190 J m^{-2} for liver) and high shear and tensile strength (more than 120 kPa for skin, 80 kPa for small intestine, 70 kPa for stomach, 80 kPa for muscle, 70 kPa for heart and 20 kPa for liver) (Fig. 2d and Supplementary Fig. 10a–c). The DST can also provide adhesion between wet tissues and various engineering solids, including hydrogel, silicon, titanium, polydimethylsiloxane (PDMS), polyimide and polycarbonate (Fig. 2e and Supplementary Video 3). We functionalize the surfaces of various engineering solids with primary amines in order to ensure covalent coupling with the DST¹⁹ (Extended Data Fig. 9), and then evaluate the adhesion performance using wet porcine skin (Supplementary Fig. 10d–f). The adhesion between the wet tissues and various engineering solids by the DST exhibits high interfacial toughness (higher than $1,150 \text{ J m}^{-2}$ for hydrogel, 800 J m^{-2} for silicon, 680 J m^{-2} for titanium, 480 J m^{-2} for PDMS, 720 J m^{-2} for polyimide and 410 J m^{-2} for

polycarbonate) and high shear and tensile strength (more than 80 kPa for hydrogel, 160 kPa for silicon, 150 kPa for titanium, 100 kPa for PDMS, 100 kPa for polyimide and 70 kPa for polycarbonate) (Fig. 2e).

In order to evaluate the ability of the DST to adhere to wet and dynamic surfaces in vivo, we adhere a thermoplastic polyurethane (TPU) patch²⁶ to the epicardial surface of a rat heart using the DST (Fig. 3a, b and Supplementary Fig. 15a). We find that a 5-mm-diameter DST-TPU hybrid patch (using the gelatin-based DST with a dry thickness of $20 \mu\text{m}$) can be adhered to the epicardial surface of a beating rat heart after gently pressing for 5 seconds (Fig. 3a and Supplementary Video 4). After 3 days of in vivo implantation, the DST-TPU patch maintains adhesion to the rat heart surface (Fig. 3b) while producing a host response similar to that of reported epicardial patches (Fig. 3c, d). Histological assessment by a blinded pathologist indicates that the degree of inflammatory reaction induced by the DST-TPU patch is comparable to that of a sutured TPU patch (Fig. 3c–e).

We further evaluate the in vivo biocompatibility and biodegradability of the DST in a rat model of dorsal subcutaneous implantation

(Fig. 3f–h and Supplementary Fig. 15b). Histological assessment demonstrates that, after 2 weeks of implantation, the chitosan-based DST (20- μ m dry thickness) generates a comparable inflammatory reaction (Fig. 3f) to that produced by Coseal, a US Food and Drug Administration (FDA)-approved, commercially available tissue adhesive (Fig. 3h). The histology at 2 weeks for both implant types is characterized by a mild to moderate chronic inflammatory response involving macrophages, lymphocytes and occasional giant cells in association with the formation of a capsule of granulation tissue comprising fibroblasts, collagen and new blood vessels. There is no evidence of necrosis of the overlying skeletal muscle or skin, or of an eosinophilic response suggestive of an allergic reaction. Although the gelatin-based DST shows a higher degree of inflammatory response than the chitosan-based DST, as indicated by a denser chronic inflammatory reaction (Fig. 3g), no major damage to the surrounding dermal and muscular layers is observed after 2 weeks of implantation. The more pronounced inflammatory response of the gelatin-based DST might result from the faster biodegradation of gelatin than of chitosan and subsequent effects on the surrounding tissues, including a higher degree of phagocytotic responses²⁷.

Furthermore, the histological images of the subcutaneously implanted DST demonstrate in vivo biodegradability of the DST (Fig. 3i–l). After two weeks of implantation, the relatively slow-degrading chitosan-based DST maintains an intact film-like configuration (Fig. 3i), while the relatively fast-degrading gelatin-based DST shows signs of degradation such as reduction in thickness and a fragmented configuration (Fig. 3j). At an implantation period of 4 weeks, the chitosan-based DST shows limited signs of degradation (Fig. 3k), whereas there is substantial continued degradation of the gelatin-based DST, as shown by increased material resorption by macrophages (Fig. 3l). In addition, there is appropriate evolution and attenuation of the inflammatory response generated by both the gelatin-based and the chitosan-based DST after 4 weeks of implantation, including a decrease in the magnitude of the chronic inflammatory infiltrate and thinning of the surrounding fibrous capsule.

In order to demonstrate potential applications of the DST, we investigate a range of proof-of-principle applications using ex vivo porcine models. The DST combined with a degradable tough hydrogel patch can form an air-tight sealing of a lacerated, air-leaking lung lobe and trachea (Fig. 4a, Extended Data Fig. 10a and Supplementary Video 5). Furthermore, it provides a fluid-tight sealing of a fluid-filled perforated stomach (with a 1-cm-wide hole) and a dissected small intestine (Fig. 4c, Extended Data Fig. 10b and Supplementary Videos 6, 7). We further show that the DST can be used to adhere devices onto dynamic and deformable tissues^{26,28–30}. For example, we use the DST to adhere a hydrogel patch with a mock drug (fluorescein) onto a beating ex vivo porcine heart (introducing cyclical, pressurized air inputs to mimic heart beats). This suggests that the DST might allow the attachment of drug-delivery devices onto dynamic wet tissues (Fig. 4d and Supplementary Video 8). The adhered DST patch maintains adhesion on the beating heart for more than 12 h without any sign of decreased adhesion and allows delivery of a mock drug into the heart tissue (Fig. 4e). As another example, we adhere a stretchable strain sensor on the beating porcine heart (Fig. 4f and Supplementary Video 9). The DST allows facile attachment of the strain sensor on the dynamic and curved surface of the beating heart, as well as electrical measurements of the heart movements (Fig. 4g). Notably, the stretchable DST–sensor hybrid is prepared by printing a conductive ink on a DST–Ecoflex hybrid substrate²⁰ (Supplementary Fig. 16). Such DST–device hybrids could serve as a versatile platform for wearable and implantable devices to adhere onto wet and dynamic tissues. Although these ex vivo models show possible applications of the DST, we note that its long-term efficacy, biocompatibility and biodegradability, as well as the induced biological responses (for example, healing) in clinically relevant settings, require further studies.

In this study, we have reported a biologically inspired, dry-crosslinking mechanism—which is implemented in the form of a dry DST—for the

adhesion of wet tissues and devices. This DST offers advantages over existing tissue adhesives and sealants, including fast adhesion formation, robust adhesion performance, flexibility, and ease of storage and use. The DST may also provide new opportunities for bioscaffolds, drug delivery, and wearable and implantable devices. This dry-crosslinking mechanism for the adhesion of wet surfaces could also be applied in the design of adhesives for wet and underwater environments.

Online content

Any methods, additional references, Nature Research reporting summaries, source data, extended data, supplementary information, acknowledgements, peer review information; details of author contributions and competing interests; and statements of data and code availability are available at <https://doi.org/10.1038/s41586-019-1710-5>.

- Creton, C. Pressure-sensitive adhesives: an introductory course. *MRS Bull.* **28**, 434–439 (2003).
- Chung, J. Y. & Chaudhury, M. K. Soft and hard adhesion. *J. Adhes.* **81**, 1119–1145 (2005).
- Peppas, N. A. & Buri, P. A. Surface, interfacial and molecular aspects of polymer bioadhesion on soft tissues. *J. Control. Release* **2**, 257–275 (1985).
- Lee, H., Lee, B. P. & Messersmith, P. B. A reversible wet/dry adhesive inspired by mussels and geckos. *Nature* **448**, 338–341 (2007).
- Reece, T. B., Maxey, T. S. & Kron, I. L. A prospectus on tissue adhesives. *Am. J. Surg.* **182**, S40–S44 (2001).
- Coulthard, P. et al. Tissue adhesives for closure of surgical incisions. *Cochrane Database Syst. Rev.* **11**, CD004287 (2014).
- Vakalopoulos, K. A. et al. Mechanical strength and rheological properties of tissue adhesives with regard to colorectal anastomosis: an ex vivo study. *Ann. Surg.* **261**, 323–331 (2015).
- Rose, S. et al. Nanoparticle solutions as adhesives for gels and biological tissues. *Nature* **505**, 382–385 (2014).
- Lee, B. P., Messersmith, P. B., Israelachvili, J. N. & Waite, J. H. Mussel-inspired adhesives and coatings. *Annu. Rev. Mater. Res.* **41**, 99–132 (2011).
- Annabi, N., Yue, K., Tamayol, A. & Khademhosseini, A. Elastic sealants for surgical applications. *Eur. J. Pharm. Biopharm.* **95**, 27–39 (2015).
- Karp, J. M. A slick and stretchable surgical adhesive. *N. Engl. J. Med.* **377**, 2092–2094 (2017).
- Li, J. et al. Tough adhesives for diverse wet surfaces. *Science* **357**, 378–381 (2017).
- LeMaire, S. A. et al. The threat of adhesive embolization: BioGlue leaks through needle holes in aortic tissue and prosthetic grafts. *Ann. Thorac. Surg.* **80**, 106–111 (2005).
- Maier, G. P., Rapp, M. V., Waite, J. H., Israelachvili, J. N. & Butler, A. Adaptive synergy between catechol and lysine promotes wet adhesion by surface salt displacement. *Science* **349**, 628–632 (2015).
- Zhao, Q. et al. Underwater contact adhesion and microarchitecture in polyelectrolyte complexes actuated by solvent exchange. *Nat. Mater.* **15**, 407–412 (2016).
- Singla, S., Amarपुरi, G., Dhoptkar, N., Blackledge, T. A. & Dhinojwala, A. Hygroscopic compounds in spider aggregate glue remove interfacial water to maintain adhesion in humid conditions. *Nat. Commun.* **9**, 1890 (2018).
- Gong, J. P., Katsuyama, Y., Kurokawa, T. & Osada, Y. Double-network hydrogels with extremely high mechanical strength. *Adv. Mater.* **15**, 1155–1158 (2003).
- Zhao, X. Multi-scale multi-mechanism design of tough hydrogels: building dissipation into stretchy networks. *Soft Matter* **10**, 672–687 (2014).
- Yuk, H., Zhang, T., Lin, S., Parada, G. A. & Zhao, X. Tough bonding of hydrogels to diverse non-porous surfaces. *Nat. Mater.* **15**, 190–196 (2016).
- Yuk, H., Zhang, T., Parada, G. A., Liu, X. & Zhao, X. Skin-inspired hydrogel–elastomer hybrids with robust interfaces and functional microstructures. *Nat. Commun.* **7**, 12028 (2016).
- Yuk, H., Lu, B. & Zhao, X. Hydrogel bioelectronics. *Chem. Soc. Rev.* **48**, 1642–1667 (2019).
- Gorgieva, S. & Kokol, V. Preparation, characterization, and in vitro enzymatic degradation of chitosan–gelatine hydrogel scaffolds as potential biomaterials. *J. Biomed. Mater. Res. A* **100A**, 1655–1667 (2012).
- Barnes, S., Spencer, M., Graham, D. & Johnson, H. B. Surgical wound irrigation: a call for evidence-based standardization of practice. *Am. J. Infect. Control* **42**, 525–529 (2014).
- Lang, N. et al. A blood-resistant surgical glue for minimally invasive repair of vessels and heart defects. *Sci. Transl. Med.* **6**, 218ra6 (2014).
- Yang, J., Bai, R. & Suo, Z. Topological adhesion of wet materials. *Adv. Mater.* **30**, 1800671 (2018).
- Whyte, W. et al. Sustained release of targeted cardiac therapy with a replenishable implanted epicardial reservoir. *Nat. Biomed. Eng.* **2**, 416–428 (2018).
- Jiang, W. W., Su, S. H., Eberhart, R. C. & Tang, L. Phagocyte responses to degradable polymers. *J. Biomed. Mater. Res. A* **82A**, 492–497 (2007).
- Yamagishi, K. et al. Tissue-adhesive wirelessly powered optoelectronic device for metronomic photodynamic cancer therapy. *Nat. Biomed. Eng.* **3**, 27–36 (2019).
- Feiner, R. et al. Engineered hybrid cardiac patches with multifunctional electronics for online monitoring and regulation of tissue function. *Nat. Mater.* **15**, 679–685 (2016).
- Roche, E. T. et al. Soft robotic sleeve supports heart function. *Sci. Transl. Med.* **9**, eaaf3925 (2017).

Publisher's note Springer Nature remains neutral with regard to jurisdictional claims in published maps and institutional affiliations.

© The Author(s), under exclusive licence to Springer Nature Limited 2019

Methods

Materials

All chemicals were obtained from Sigma-Aldrich unless otherwise mentioned, and used without further purification. To prepare the DST, we used acrylic acid, gelatin methacrylate (gelMA; type A bloom 90-100 from porcine skin with 60% substitution), acrylic acid *N*-hydroxysuccinimide ester (AAc-NHS ester), α -ketoglutaric acid, gelatin (type A bloom 300 from porcine skin) and chitosan (75–85% deacetylated). To visualize the DST in photographs and microscope images, we used red food dye (McCormick) and fluorescein isothiocyanate (FITC)–gelatin (Thermo Fisher Scientific). For *in vitro* biodegradation tests, we used Dulbecco's phosphate-buffered saline (DPBS, with calcium and magnesium; Gibco), collagenase, lysozyme and NAGase. To prepare the degradable tough hydrogel, we used acrylamide, gelatin, gelMA, and Irgacure 2959. For surface functionalization of engineering solids, we used (3-aminopropyl) triethoxysilane (APTES) and hexamethyldiamine (HMDA). To prepare the stretchable strain sensor, we used Ecoflex 00-30 (Smooth-On), silicone curing retardant (SLO-JO, Smooth-On) and carbon black (Alfa Aesar). All engineering solids were obtained from McMaster Carr unless otherwise mentioned. All porcine tissues for *ex vivo* experiments were purchased from a research-grade porcine tissue vendor (Sierra Medical).

Preparation of the dry DST

The DST was prepared with either gelatin or chitosan. To prepare the gelatin-based DST, we dissolved 30% (w/w) acrylic acid, 10% (w/w) gelatin, 1% (w/w) AAc-NHS ester, 0.1% (w/w) gelMA and 0.2% (w/w) α -ketoglutaric acid in deionized water. The mixture was then filtered with 0.4- μ m sterile syringe filters and poured on a glass mould with spacers. The DST was cured in an ultraviolet light (UV) chamber (284 nm, 10 W power) for 20 min and completely dried. The final DST was sealed in plastic bags with desiccant (silica gel packets) and stored at -20°C before use. The chitosan-based DST was prepared by replacing 10% (w/w) gelatin with 2% (w/w) chitosan. In experiments, we used the gelatin-based DST with an as-prepared thickness of 210 μ m unless otherwise mentioned. To prepare the DST in various shapes, we cut a large sheet of DST into each design using a laser cutter (Epilog). Polyethylene-coated paper was used as a backing for the DST. To aid visualization of the DST, we added 0.5% (w/w) of red food dye (for photographs) or 0.2% (w/w) FITC–gelatin (for fluorescence microscopy images) into the precursor solution before curing.

Mechanical tests

Tissue samples stored more than 10 min before mechanical tests were covered with an excess of 0.01% (w/v) sodium azide solution (in PBS) spray and sealed in plastic bags to prevent degradation and dehydration. Unless otherwise indicated, all tissues and engineering solids were adhered by the DST after washing out the surfaces with PBS followed by 5 seconds of pressing (with 1 kPa pressure applied by either a mechanical testing machine or an equivalent weight). Unless otherwise indicated, all mechanical tests on adhesion samples were performed 24 h after initial pressing to ensure equilibrium swelling of the adhered DST in wet environments. The application of commercially available tissue adhesives followed the manual provided for each product. The gelatin-based DST was used unless otherwise noted.

To measure interfacial toughness, adhered samples with widths of 2.5 cm were prepared and tested by the standard 180-degree peel test (ASTM F2256) or 90-degree peel test (ASTM D2861) (for inflexible substrates such as silicon) using a mechanical testing machine (2.5 kN load-cell, Zwick/Roell Z2.5). All tests were conducted with a constant peeling speed of 50 mm min⁻¹. The measured force reached a plateau as the peeling process entered the steady state. Interfacial toughness was determined by dividing two times the plateau force (for a 180-degree peel test) or the plateau force (for a 90-degree peel test)

by the width of the tissue sample (Extended Data Fig. 6a). Poly(methyl methacrylate) films (with a thickness of 50 μ m; Goodfellow) were applied using cyanoacrylate glue (Krazy Glue) as a stiff backing for the tissues and hydrogels.

To measure shear strength, adhered samples with an adhesion area of width 2.5 cm and length 1 cm were prepared and tested by the standard lap-shear test (ASTM F2255) with a mechanical testing machine (2.5 kN load-cell, Zwick/Roell Z2.5) (Extended Data Fig. 6b). All tests were conducted with a constant tensile speed of 50 mm min⁻¹. Shear strength was determined by dividing the maximum force by the adhesion area. Poly(methyl methacrylate) films were applied using cyanoacrylate glue to act as a stiff backing for the tissues and hydrogels.

To measure tensile strength, adhered samples with adhesion areas of width 2.5 cm and length 2.5 cm were prepared and tested by the standard tensile test (ASTM F2258) with a mechanical testing machine (2.5 kN load-cell, Zwick/Roell Z2.5) (Extended Data Fig. 6c). All tests were conducted with a constant tensile speed of 50 mm min⁻¹. Tensile strength was determined by dividing the maximum force by the adhesion area. Aluminium fixtures were applied using cyanoacrylate glues to provide grips for tensile tests.

To characterize mechanical properties of the swollen DST, the DST was equilibrated in PBS before tests. The tensile properties and fracture toughness of the DST were measured using pure-shear tensile tests of thin rectangular samples (10 mm in length, 30 mm in width and 0.5 mm in thickness) with a mechanical testing machine (20 N load-cell, Zwick/Roell Z2.5). All tests were conducted with a constant tensile speed of 50 mm min⁻¹. The fracture toughness of the DST was calculated using a reported method based on tensile tests of unnotched and notched samples¹².

To characterize the adhesion performance of the DST under cyclic loading, two porcine heart tissues were adhered by the DST with an adhesion area of width 2.5 cm and length 4 cm. Each side of the adhered tissues was cyclically stretched at 30% tensile strain (with respect to the DST length) using a mechanical testing machine (2.5 kN load-cell, Zwick/Roell Z2.5) to provide cyclic shear loading to the adhesion interface (Supplementary Fig. 13). Interfacial toughness between the heart tissues adhered by the DST was measured at different cycle numbers by the standard 180-degree peel test (ASTM F2256). During the cyclic tests, a 0.01% (w/v) sodium azide solution (in PBS) was sprayed onto the heart tissues to avoid tissue degradation and dehydration.

Preparation of engineering solids

To prepare degradable tough hydrogels for adhesion tests of engineering solids, we dissolved 20% (w/w) acrylamide, 10% (w/w) gelatin, 0.2% (w/w) gelMA and 0.2% (w/w) Irgacure 2959 in deionized water. The mixture was then filtered with 0.4- μ m sterile syringe filters and poured on a glass mould with spacers. The hydrogels were cured in a UV chamber (284 nm, 10 W power) for 60 min. To facilitate covalent coupling with the DST, engineering solids except hydrogel were functionalized with primary amines (Extended Data Fig. 9). For silicon, titanium and PDMS, the substrates were first treated with oxygen plasma for 2 min (30 W power, Harrick Plasma) to activate the surface. Subsequently, the plasma-treated substrates were covered with APTES solution (1% (w/w) APTES in 50% ethanol) and incubated for 3 h at room temperature²⁰. The substrates were then thoroughly washed with isopropyl alcohol and dried using a nitrogen flow. For polyimide and polycarbonate, the substrates were immersed into the HMDA solution (10% (v/v) in deionized water) for 24 h at room temperature. The substrates were then thoroughly washed with deionized water and dried using a nitrogen flow³¹.

In vitro biocompatibility tests

We conducted *in vitro* biocompatibility tests using DST-conditioned medium for cell culture³². To prepare the DST-conditioned medium for *in vitro* biocompatibility tests, we incubated 20 mg of the gelatin-based DST in 1 ml of Dulbecco's modified Eagle medium (DMEM) at 37 $^{\circ}\text{C}$

Article

for 24 h. Pristine DMEM was used as a control. Wild-type MEFs were plated in 96-well plates ($n=10$ for DST-conditioned medium; $n=10$ for DMEM). The cells were then treated with the DST-conditioned medium and incubated at 37 °C for 24 h in 5% CO₂. Cell viability was determined with a live/dead viability/cytotoxicity kit for mammalian cells (Thermo Fisher Scientific) by adding 4 μ M calcein and ethidium homodimer-1 into the culture medium. We used a confocal microscope (SP 8, Leica) to image live cells with excitation/emission at 495 nm/515 nm, and dead cells at 495 nm/635 nm.

In vitro biodegradation tests

We carried out in vitro biodegradation tests of the DST using enzymatic degradation media as described²². To prepare in vitro enzymatic biodegradation medium for the gelatin-based DST, we added 5 mg collagenase in 100 ml DPBS. To prepare in vitro enzymatic biodegradation medium for the chitosan-based DST, we added 5 mg collagenase, 5 mg lysozyme and 10 μ l of 1 mg ml⁻¹ NAGase aqueous solution in 100 ml DPBS. The DST was cut into small samples (of width 10 mm and length 10 mm) and accurately weighed. Before immersion in the enzymatic media, the samples were sterilized in 75% ethanol for 15 min and washed three times with DPBS. Each sample was then immersed in 15 ml of the enzymatic medium within glass scintillation vials and incubated at 37 °C with shaking at 60 r.p.m. About 0.01% (w/v) sodium azide was added into the enzymatic media to prevent growth of any microorganisms during the tests. At each time interval, the DST was removed from the incubation medium, exhaustively washed with deionized water and lyophilized. Weight loss was determined as the percentage ratio of the mass of the lyophilized sample at each time interval, normalized by the dry mass of the original lyophilized sample.

In vivo adhesion, biocompatibility and biodegradability tests

All animal procedures were reviewed and approved by the Massachusetts Institute of Technology Committee on Animal Care. Details of surgical procedures and in vivo data analysis are provided in the Supplementary Information.

Preparation of the DST–strain-sensor hybrid

We prepared the DST–strain-sensor hybrid by printing a conductive ink onto a DST–elastomer hybrid substrate. This elastomer substrate was first prepared by casting Ecoflex 00-30 resin mixture (part A and part B in a 1/1 volume ratio) into a laser-cut acrylic mould. Subsequently, a thin layer of gelatin-based DST (100- μ m dry thickness) was introduced on the bottom side of the Ecoflex substrate according to the reported protocol for hydrogel–elastomer hybrids²¹. The strain sensor was fabricated by printing the conductive ink onto the DST–Ecoflex hybrid substrate using a custom direct ink writing (DIW) 3D printer³³. Briefly, the conductive ink was prepared by mixing 10% (w/w) carbon black and 1% (w/w) silicone curing retardant into Ecoflex 00-30 resin (part A and part B in a 1/1 volume ratio) using a planetary mixer (AR-100, Thinky). The printing paths were generated through production of G-codes that control the XYZ motions of a robotic gantry (Aerotech). We used a pressure-based microdispenser (Ultimus V, Nordson EFD) with a 200- μ m-diameter nozzle (Smoothflow tapered tip, Nordson EFD) to print the conductive ink on the substrate through a custom LabVIEW interface (National Instruments). Deformation-induced changes in the electrical resistance of the strain sensor were monitored with a digital multimeter (34450A, Keysight).

HPLC characterization of the DST

We analysed the residual monomer contents of the DST using analytical high-performance liquid chromatography (HPLC; Model 1100, Agilent). We used 0.1% phosphoric acid as the mobile phase, extractant and medium for an acrylic acid monomer standard solution as described³⁴ (Extended Data Fig. 5). To extract the residual monomer from the DST, we incubated 100 mg of the DST in 20 ml of the extractant for 24 h with

stirring. After the extraction, the solution was filtered with a sterile 0.2- μ m syringe filter and injected into the HPLC system for analysis. The concentration of the residual acrylic acid monomer in the DST was determined on the basis of the calibration curve obtained from the standard solution diluted with the mobile phase to varying monomer concentrations.

FTIR characterization of the DST

The chemical composition of the DST was characterized using a transmission Fourier transform infrared spectroscope (FTIR 6700, Thermo Fisher) with a germanium-attenuated total reflectance (ATR) crystal (55 degrees). The FTIR spectrum of the DST was analysed as described^{35,36} (Extended Data Fig. 2a).

Ex vivo tests

All ex vivo experiments were reviewed and approved by the Committee on Animal Care at the Massachusetts Institute of Technology. To assess sealing of damaged trachea, we made a laceration (1.5 cm in length) in a porcine trachea using a razor blade. Air was then applied through tubing connected to the upper part of the trachea (25 mm Hg pressure) to visualize air leakage from the trachea submerged in a water bath. To seal the laceration, we adhered a hydrogel patch (of width 2.5 cm and length 5 cm) to the damaged trachea using the DST with 5 seconds of pressing. The sealed porcine trachea was kept for 12 h at room temperature with continuous inflation–deflation cycles to monitor the DST-based sealing. We added 0.01% (w/v) sodium azide into the water bath to avoid tissue degradation.

To assess sealing of a damaged lung lobe, we made a laceration (3 cm long) in a porcine lung lobe with a razor blade. Air was then applied through tubing connected to the upper part of the trachea (25 mm Hg pressure) in order to visualize air leakage from the lung lobe submerged in the water bath. To seal the laceration, we adhered a hydrogel patch (of width 2.5 cm and length 5 cm) to the damaged lung lobe using the DST with 5 seconds of pressing. The sealed porcine lung lobe was kept for 12 h at room temperature with continuous inflation–deflation cycles to monitor the DST-based sealing. We added 0.01% (w/v) sodium azide into the water bath to avoid tissue degradation.

To assess sealing of damaged stomach, we punched a 10-mm-wide hole in a porcine stomach. A tube with flowing water was then connected to the upper part of the stomach to visualize fluid leakage from the stomach. To seal the hole, we adhered a 40-mm-wide hydrogel patch onto the damaged stomach using the DST with 5 seconds of pressing. The sealed porcine stomach was kept for 12 h at room temperature to monitor the DST-based sealing. We sprayed 0.01% (w/v) sodium azide solution (in PBS) onto the porcine stomach to avoid tissue degradation.

To assess sealing of an anastomosis site in a small intestine, we dissected a porcine small intestine into two pieces. Anastomosis of the dissected small intestine was made by approximating each edge of the small intestine followed by wrapping of the DST (2.5 cm wide and 8 cm long) and 5 seconds of pressing around the approximated edges. To check that the DST had produced fluid-tight sealing, we applied water to the anastomosed small intestine at 60 mm Hg pressure using a microdispenser. We sprayed 0.01% (w/v) sodium azide solution (in PBS) onto the porcine small intestine to avoid tissue degradation.

To assess the adhesion of a drug-delivery device, we introduced a cut (4 cm in length) on an explanted porcine heart. The aorta was connected to tubing, and programmed pressurized air inputs were introduced into the heart using a microdispenser to mimic heart beats. To prepare the drug-delivery device, we added 0.5% (w/w) fluorescein sodium salt as a mock drug into a hydrogel patch (2.5 cm in width and 5 cm in length). The drug-loaded hydrogel patch was then stretched to fit the cut and adhered onto the beating porcine heart with the perforated DST. The adhered drug patch on the beating heart was kept for 12 h

at room temperature with continuous beating to allow diffusion of the mock drug into the heart tissue. The diffusion of the mock drug was imaged using a fluorescence microscope (LV100ND, Nikon). To assess the adhesion of a strain sensor, we adhered the DST–strain-sensor hybrid onto the beating porcine heart after removing the backing. The adhered strain sensor on the beating heart was kept for 12 h at room temperature with continuous beating, and then connected with the digital multimeter to monitor the deformation of the beating heart. All devices were adhered onto the beating heart after washing out the surfaces with PBS, followed by 5 seconds of pressing. To prevent dehydration and degradation during experiments of longer than 1 h in ambient conditions, we covered the heart with a wet towel soaked with 0.01% (w/v) sodium azide solution (in PBS).

Reporting summary

Further information on research design is available in the Nature Research Reporting Summary linked to this paper.

Data availability

All data are available in the main text or the Supplementary Information.

31. VanDelinder, V. et al. Simple, benign, aqueous-based amination of polycarbonate surfaces. *ACS Appl. Mater. Interfaces* **7**, 5643–5649 (2015).
32. Darnell, M. C. et al. Performance and biocompatibility of extremely tough alginate/polyacrylamide hydrogels. *Biomaterials* **34**, 8042–8048 (2013).
33. Yuk, H. & Zhao, X. A new 3D printing strategy by harnessing deformation, instability, and fracture of viscoelastic inks. *Adv. Mater.* **30**, 1704028 (2018).
34. Jamshidi, A., Beigi, F. A. K., Kabiri, K. & Zohuriaan-Mehr, M. Optimized HPLC determination of residual monomer in hygienic SAP hydrogels. *Polym. Test.* **24**, 825–828 (2005).
35. Wang, C., Yan, Q., Liu, H.-B., Zhou, X.-H. & Xiao, S.-J. Different EDC/NHS activation mechanisms between PAA and PMAA brushes and the following amidation reactions. *Langmuir* **27**, 12058–12068 (2011).
36. Lim, C. Y. et al. Succinimidyl ester surface chemistry: implications of the competition between aminolysis and hydrolysis on covalent protein immobilization. *Langmuir* **30**, 12868–12878 (2014).

Acknowledgements We thank J. Hu and M. Guo in the Massachusetts Institute of Technology (MIT) Mechanical Engineering Department for their help with the cell viability test; T. McClure in the MIT Materials Research Laboratory for help with the FTIR measurement; and S. Ngoy in the Brigham and Women's Hospital (BWH) Rodent Cardiovascular Physiology Core for technical support with rodent surgery. This work is supported by the US National Science Foundation (NSF; grant CMMI-1661627) and Office of Naval Research (N00014-17-1-2920). H.Y. acknowledges financial support from a Samsung Scholarship. C.E.V. acknowledges financial support from the NSF Graduate Research Fellowship Program.

Author contributions H.Y. conceived the idea. H.Y. developed the materials and methods for the DST. H.Y. and C.S.N. designed the in vitro and ex vivo experiments. H.Y. conducted the in vitro and ex vivo experiments. C.E.V., H.Y. and E.T.R. designed the in vivo experiments. C.E.V. and H.Y. conducted the in vivo experiments. X.M., H.Y. and X.Z. developed the quantitative model for the DST. R.F.P. conducted histological assessments. H.Y., C.E.V., R.F.P., E.T.R. and X.Z. analysed the results. H.Y. and X.Z. wrote the manuscript with input from all authors. X.Z. supervised the study.

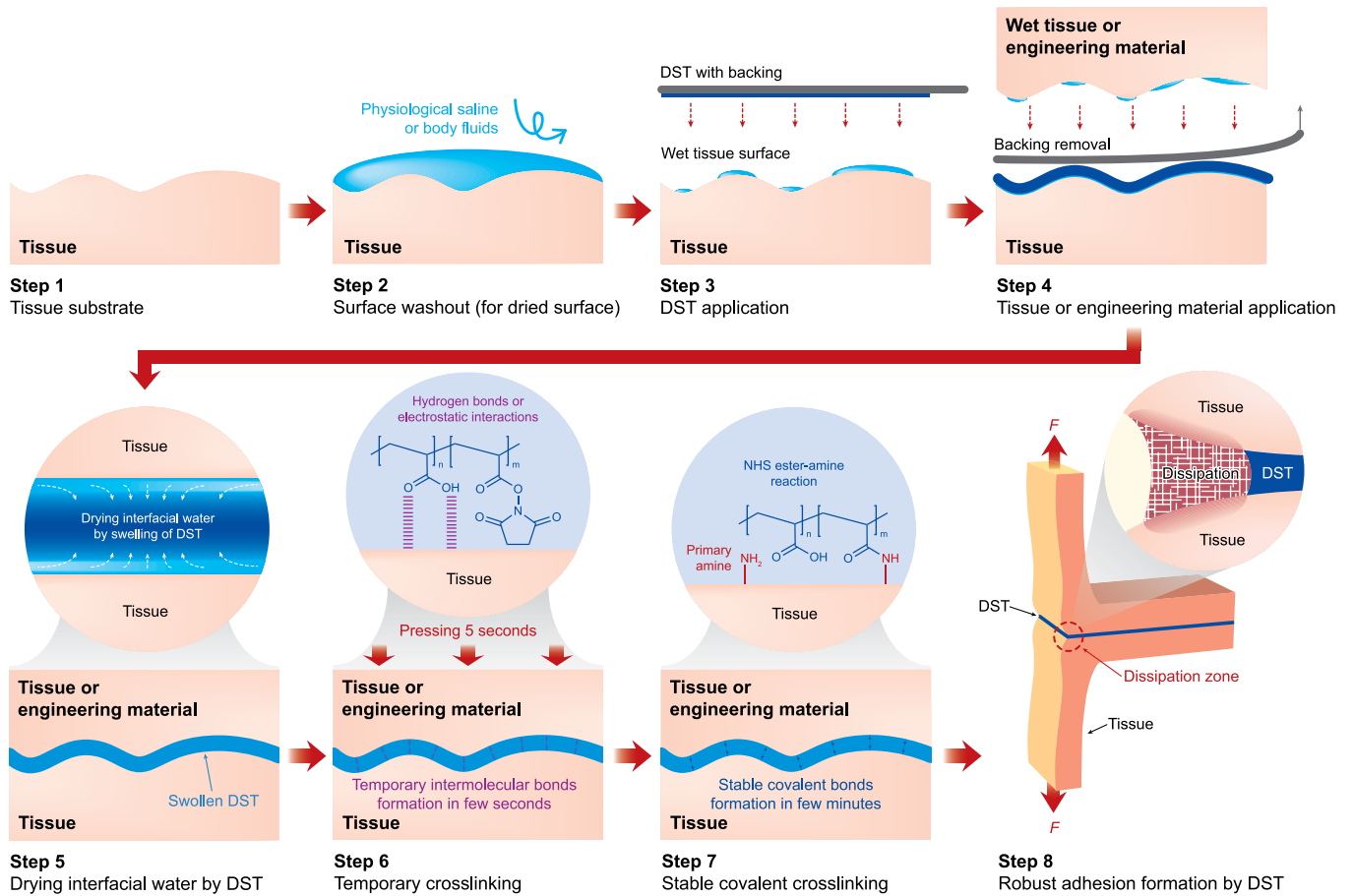
Competing interests H.Y. and X.Z. are inventors of a patent application (US patent 62/845,976) that covers the dry-crosslinking mechanism and the design of DST.

Additional information

Supplementary information is available for this paper at <https://doi.org/10.1038/s41586-019-1710-5>.

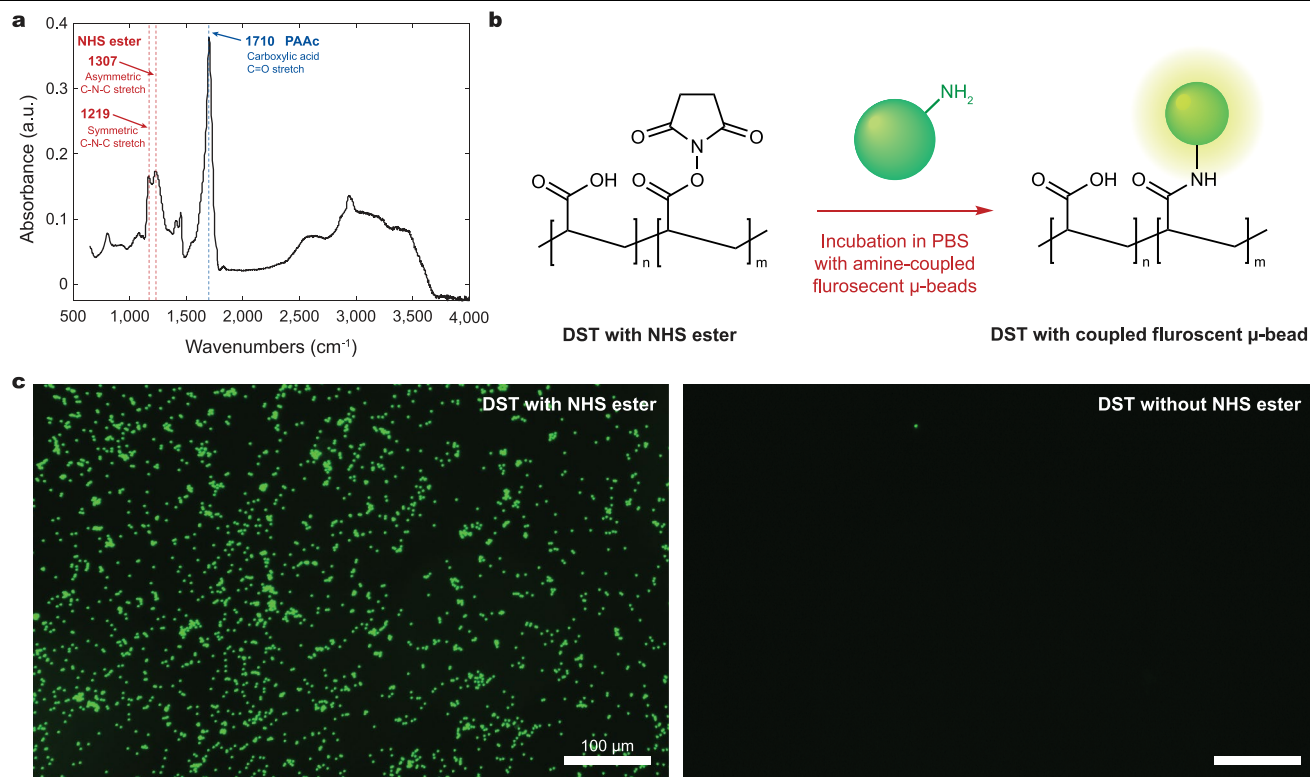
Correspondence and requests for materials should be addressed to X.Z.

Reprints and permissions information is available at <http://www.nature.com/reprints>.



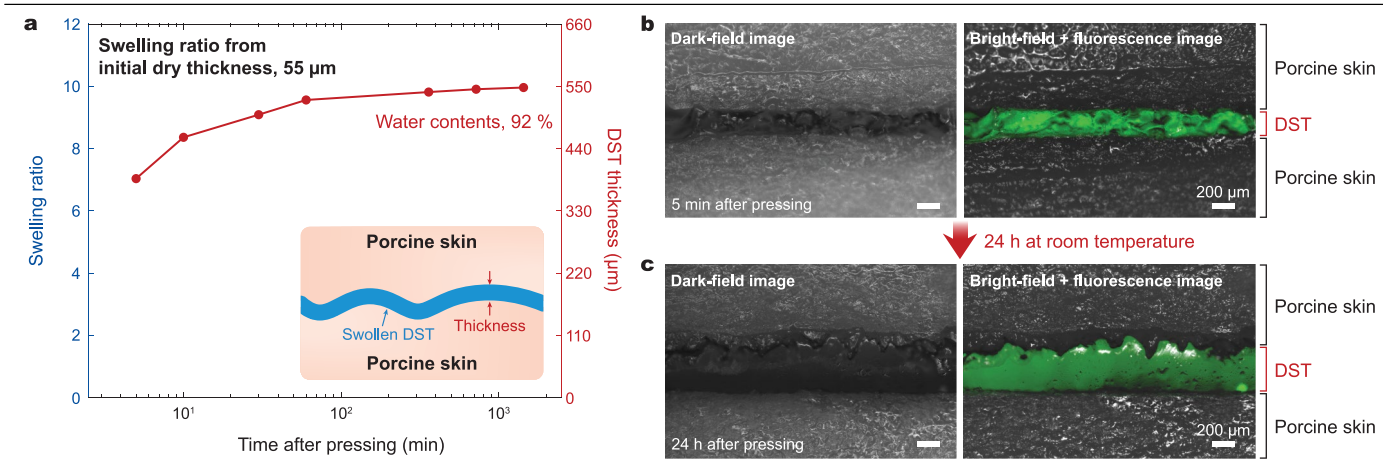
Extended Data Fig. 1 | The overall process of DST application. The DST can be applied directly onto wet tissue surfaces after removing the backing, without any other preparation process. Upon contact with the wet surfaces, the DST dries them by quickly swelling and absorbing the interfacial water. Simultaneously, the carboxylic acid groups in the DST form temporary crosslinks through intermolecular bonds with the tissue surfaces, followed by

covalent crosslinking between NHS ester groups in the DST and primary amine groups on the tissues. After adhering on tissues, the swollen DST becomes a thin layer of tough hydrogel which provides robust adhesion between the surfaces. Dissipation indicates the mechanical energy dissipation from the DST during deformation by the applied force, F .



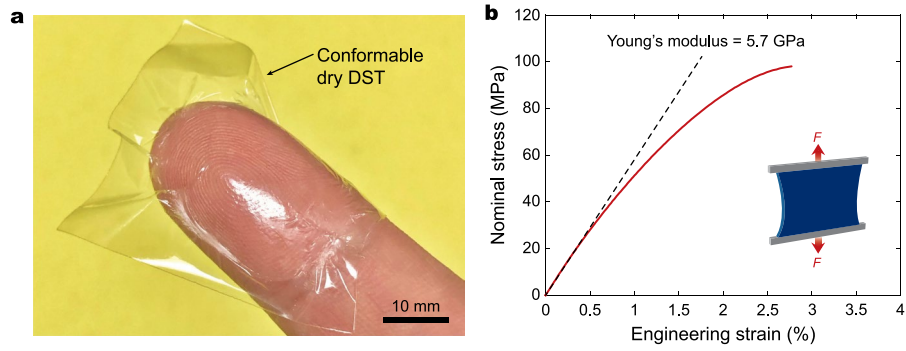
Extended Data Fig. 2 | Presence of NHS ester and surface amine coupling of the DST. a, Transmission FTIR spectrum of the DST with NHS ester. The carboxylic acid C=O stretch at $1,710\text{ cm}^{-1}$ is associated with PAAc in the DST. The symmetric C–N–C stretch at $1,219\text{ cm}^{-1}$ and asymmetric C–N–C stretch at $1,307\text{ cm}^{-1}$ are associated with NHS ester in the DST^{35,36}. **b**, Schematic

illustration of covalent crosslinking between amine-coupled fluorescent microbeads (μ -beads) with the DST. **c**, Fluorescence microscopy images of covalently crosslinked microbeads with DST with NHS ester (left) and DST without NHS ester (right).

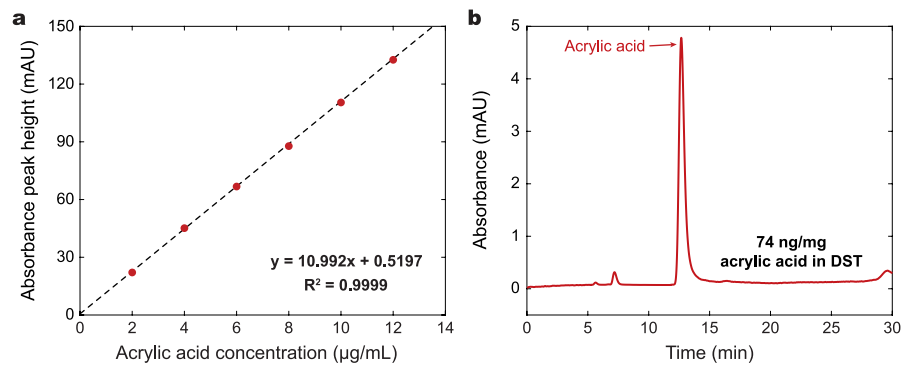


Extended Data Fig. 3 | Swelling of the DST. **a**, Swelling ratio and thickness of the chitosan-based DST as a function of time after pressing between two wet porcine skins. **b**, Dark-field microscopic image and bright-field image overlaid with green fluorescence of porcine skins adhered by the chitosan-based DST

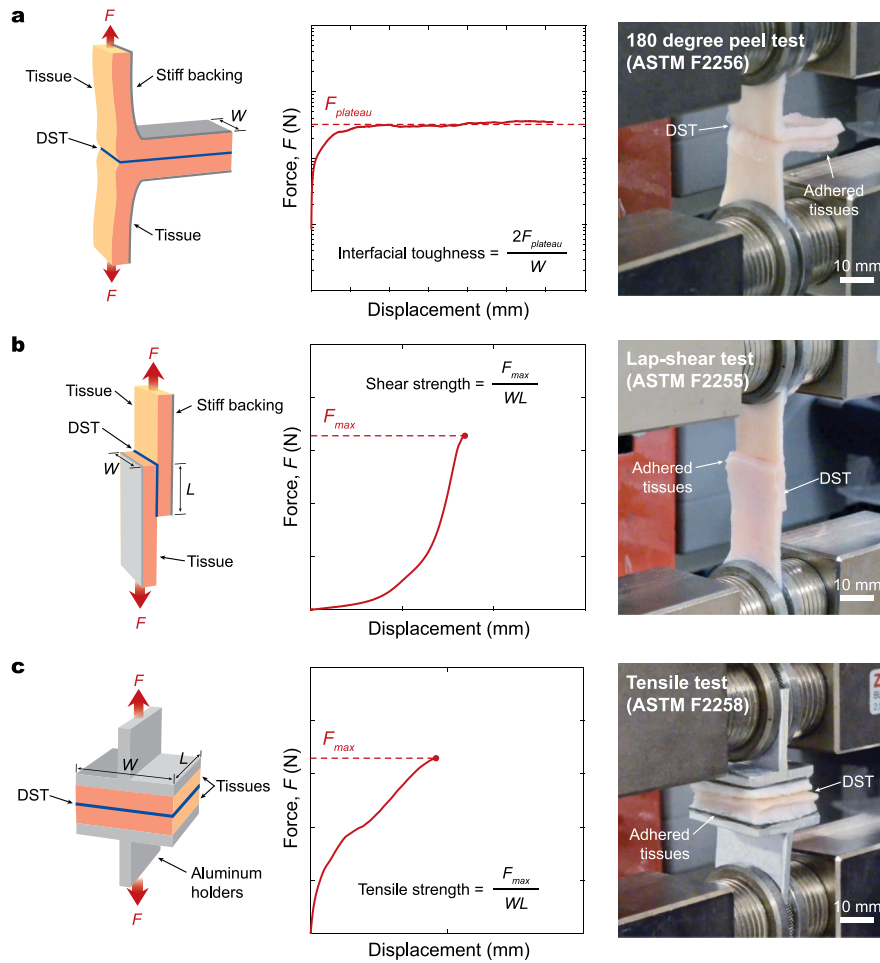
5 min after application. **c**, Dark-field microscopic image and bright-field image overlaid with green fluorescence of porcine skins adhered by the chitosan-based DST 24 h after application. The sample was kept in a wet environment throughout the measurement.



Extended Data Fig. 4 | Properties of the dry DST. **a**, The DST is initially prepared as a thin dry film that can conform to tissue surfaces. **b**, Nominal stress versus engineering strain for the dry DST. The measured Young's modulus of the dry DST is 5.7 GPa.

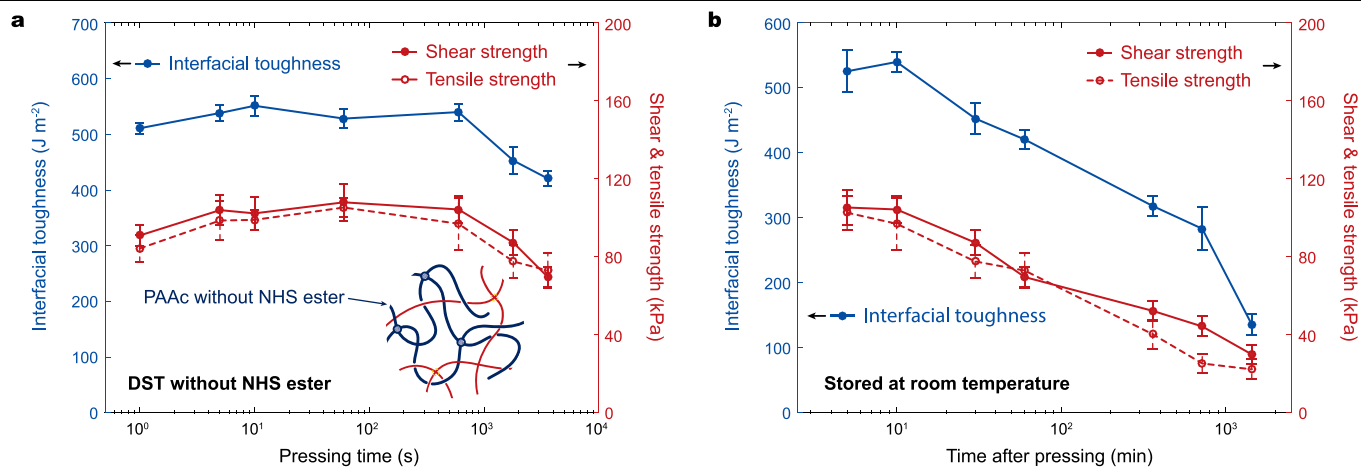


Extended Data Fig. 5 | Quantification of residual monomer in the DST by HPLC. **a**, Standard calibration curve of acrylic acid for HPLC. **b**, Results of HPLC characterization of the DST extraction solution. The DST has a very low concentration of residual acrylic acid monomers: 74 ng per 1 mg of the DST.



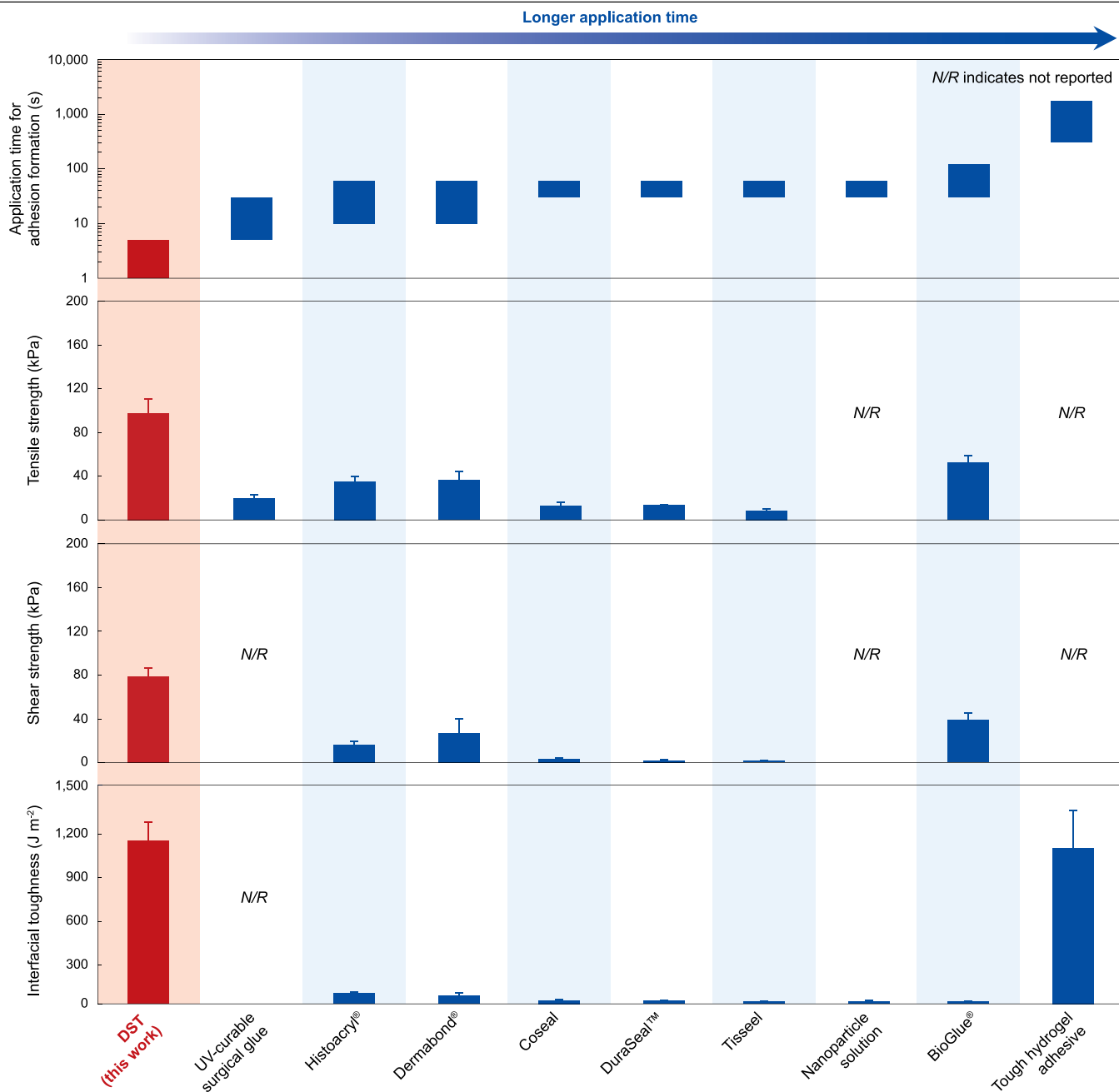
Extended Data Fig. 6 | Setups for mechanical testing of adhesion performance. **a**, Setup for measurement of interfacial toughness, based on the standard 180-degree peel test (ASTM F2256). **b**, Setup for measurement of shear strength, based on the standard lap-shear test (ASTM F2255). **c**, Setup for

measurement of tensile strength, based on the standard tensile test (ASTM F2258). F , force; F_{plateau} , plateau force in peel test; F_{max} , maximum force in lap-shear and tensile test; L , length; W , width.



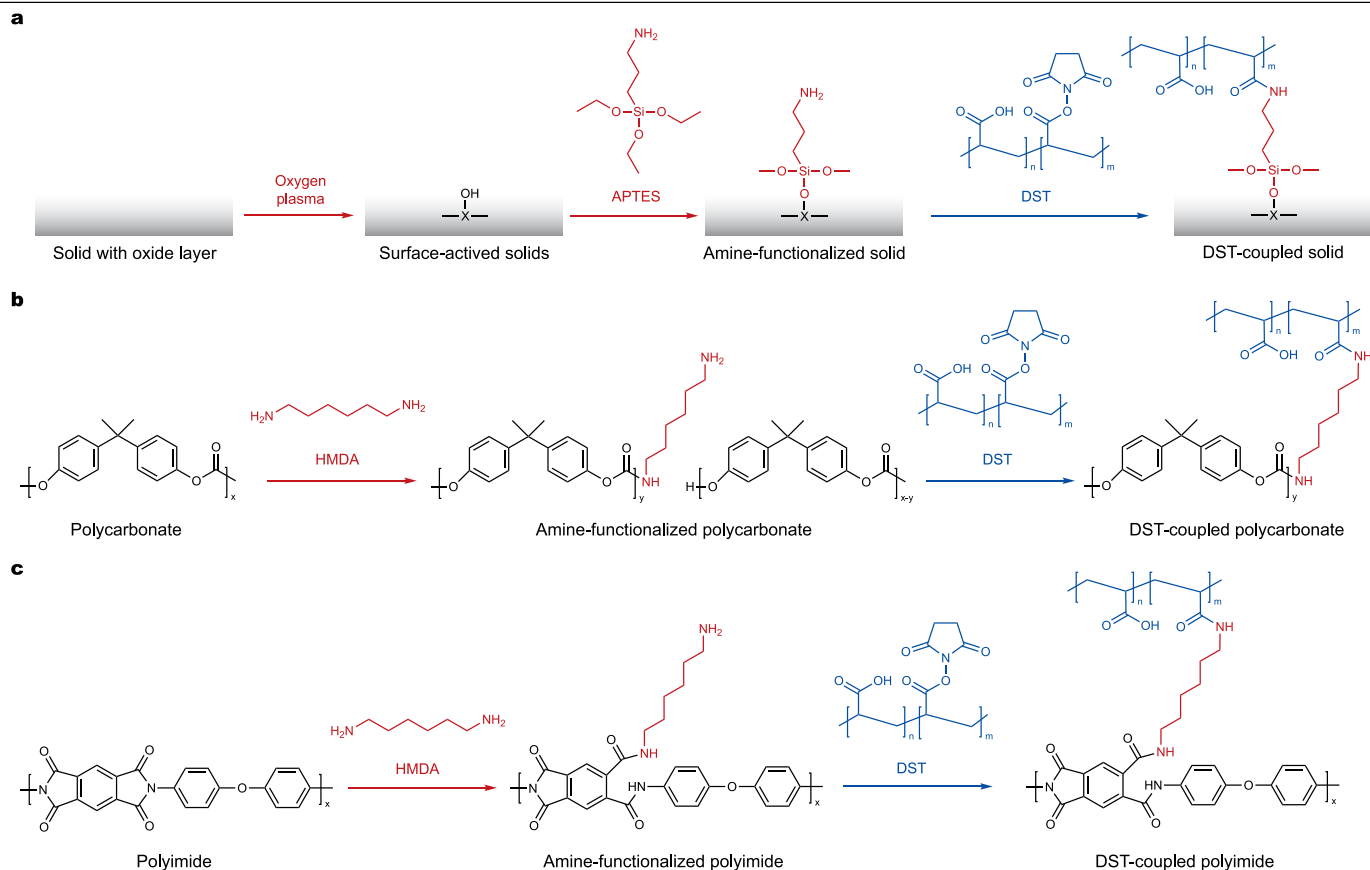
Extended Data Fig. 7 | Effect of covalent crosslinks on the long-term stability of adhesion by the DST. a, Interfacial toughness and shear and tensile strength versus pressing time for wet porcine skins adhered by the DST without NHS ester. Note that these adhesion tests were performed immediately after the initial pressing. **b,** Interfacial toughness and shear and tensile strength

versus time after pressing for wet porcine skins adhered by the DST without NHS ester. Note that all samples for **b** were kept in wet environments before the mechanical tests. Values represent the mean and the standard deviation ($n = 3-5$).



Extended Data Fig. 8 | Adhesion performances of the DST and various existing tissue adhesives. Shown are typical values for interfacial toughness, shear and tensile strength, and application time required for adhesion formation, for the DST (adhered between hydrogel and porcine skin) and various existing tissue adhesives. The interfacial toughness, shear strength and tensile strength for all commercially available adhesives were measured

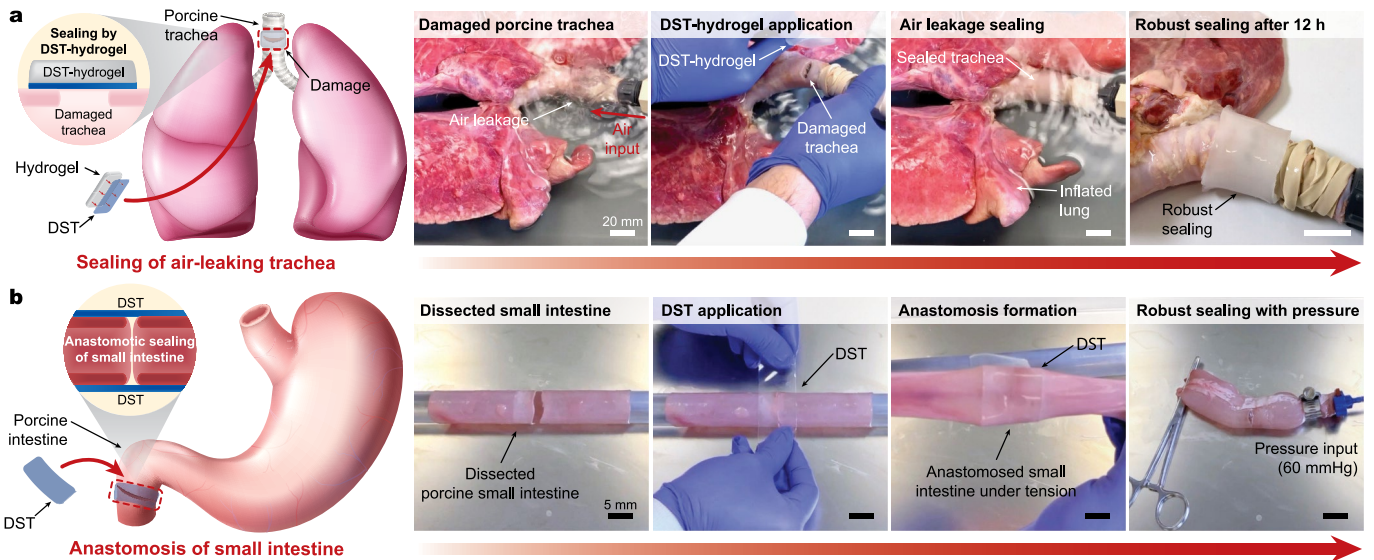
according to the application manual provided for each product. The application time for commercially available adhesives was based on the application manuals provided. The data for ultraviolet-curable surgical glue²⁴, nanoparticle solution⁸ and tough hydrogel adhesive¹² were obtained from the literature. Values represent the mean and the standard deviation ($n = 3-5$).



Extended Data Fig. 9 | Surface functionalization of engineering solids.

a, Primary amine functionalization of silicon, titanium and PDMS, and subsequent covalent coupling between the primary amine groups and the NHS ester groups in the DST. **b**, Primary amine functionalization of polycarbonate,

and subsequent covalent coupling between the primary amine groups and the NHS ester groups in the DST. **c**, Primary amine functionalization of polyimide, and subsequent covalent coupling between the primary amine groups and the NHS ester groups in the DST.



Extended Data Fig. 10 | Sealing of ex vivo porcine trachea and small intestine by the DST. a, Sealing of an air-leaking, lacerated ex vivo porcine trachea by a hydrogel patch adhered by the DST. **b,** Anastomosis of a dissected ex vivo porcine small intestine by the DST.

Reporting Summary

Nature Research wishes to improve the reproducibility of the work that we publish. This form provides structure for consistency and transparency in reporting. For further information on Nature Research policies, see [Authors & Referees](#) and the [Editorial Policy Checklist](#).

Statistics

For all statistical analyses, confirm that the following items are present in the figure legend, table legend, main text, or Methods section.

n/a Confirmed

- ☐ ☒ The exact sample size (n) for each experimental group/condition, given as a discrete number and unit of measurement
- ☐ ☒ A statement on whether measurements were taken from distinct samples or whether the same sample was measured repeatedly
- ☐ ☒ The statistical test(s) used AND whether they are one- or two-sided
Only common tests should be described solely by name; describe more complex techniques in the Methods section.
- ☐ ☒ A description of all covariates tested
- ☐ ☒ A description of any assumptions or corrections, such as tests of normality and adjustment for multiple comparisons
- ☐ ☒ A full description of the statistical parameters including central tendency (e.g. means) or other basic estimates (e.g. regression coefficient) AND variation (e.g. standard deviation) or associated estimates of uncertainty (e.g. confidence intervals)
- ☒ ☐ For null hypothesis testing, the test statistic (e.g. F , t , r) with confidence intervals, effect sizes, degrees of freedom and P value noted
Give P values as exact values whenever suitable.
- ☒ ☐ For Bayesian analysis, information on the choice of priors and Markov chain Monte Carlo settings
- ☒ ☐ For hierarchical and complex designs, identification of the appropriate level for tests and full reporting of outcomes
- ☒ ☐ Estimates of effect sizes (e.g. Cohen's d , Pearson's r), indicating how they were calculated

Our web collection on [statistics for biologists](#) contains articles on many of the points above.

Software and code

Policy information about [availability of computer code](#)

Data collection

No software used for data collection.

Data analysis

All data analyses have conducted by using custom codes based on MATLAB.

For manuscripts utilizing custom algorithms or software that are central to the research but not yet described in published literature, software must be made available to editors/reviewers. We strongly encourage code deposition in a community repository (e.g. GitHub). See the Nature Research [guidelines for submitting code & software](#) for further information.

Data

Policy information about [availability of data](#)

All manuscripts must include a [data availability statement](#). This statement should provide the following information, where applicable:

- Accession codes, unique identifiers, or web links for publicly available datasets
- A list of figures that have associated raw data
- A description of any restrictions on data availability

All data is available in the main text or the supplementary information.

Field-specific reporting

Please select the one below that is the best fit for your research. If you are not sure, read the appropriate sections before making your selection.

- ☒ Life sciences ☐ Behavioural & social sciences ☐ Ecological, evolutionary & environmental sciences

For a reference copy of the document with all sections, see nature.com/documents/nr-reporting-summary-flat.pdf

Life sciences study design

All studies must disclose on these points even when the disclosure is negative.

Sample size	Ex vivo experiments on porcine organs and tissues were conducted to evaluate adhesion performance of the DST. The appropriate sample size (n=3-5) was used for each test. In vivo experiments on rat were conducted to investigate in vivo biocompatibility and biodegradability based on histological assessment after implantation. The appropriate sample size (n=3) was used to evaluate biocompatibility and biodegradability of each sample.
Data exclusions	No data was excluded for ex vivo experiments. The following rats were also excluded: Animals that did not survive the surgery, animals that showed infection or opened the sutured incision, and animals with defective samples.
Replication	Ex vivo studies for mechanical characterization of the DST were reliably reproduced. The average and standard deviation were reported for each test. In vivo studies for biocompatibility and biodegradability were reliably reproduced based on similar histological assessment for each case by the blinded pathologist. Adhesion performance was compromised when sample was defective due to expired chemical.
Randomization	No formal randomization was used but surgeries were carried out on groups, which were alternated. Each group was completed over 2-3 different surgery days.
Blinding	All histological assessments were conducted by the blinded pathologist without informing type or group of samples.

Reporting for specific materials, systems and methods

We require information from authors about some types of materials, experimental systems and methods used in many studies. Here, indicate whether each material, system or method listed is relevant to your study. If you are not sure if a list item applies to your research, read the appropriate section before selecting a response.

Materials & experimental systems

n/a	Involved in the study
<input checked="" type="checkbox"/>	<input type="checkbox"/> Antibodies
<input checked="" type="checkbox"/>	<input type="checkbox"/> Eukaryotic cell lines
<input checked="" type="checkbox"/>	<input type="checkbox"/> Palaeontology
<input type="checkbox"/>	<input checked="" type="checkbox"/> Animals and other organisms
<input checked="" type="checkbox"/>	<input type="checkbox"/> Human research participants
<input checked="" type="checkbox"/>	<input type="checkbox"/> Clinical data

Methods

n/a	Involved in the study
<input checked="" type="checkbox"/>	<input type="checkbox"/> ChIP-seq
<input checked="" type="checkbox"/>	<input type="checkbox"/> Flow cytometry
<input checked="" type="checkbox"/>	<input type="checkbox"/> MRI-based neuroimaging

Animals and other organisms

Policy information about [studies involving animals](#); [ARRIVE guidelines](#) recommended for reporting animal research

Laboratory animals	For ex vivo studies, porcine organs and tissues were purchased and used from Sierra Medical Inc. (Whittier, CA). For in vivo studies, female Sprague Dawley rats, aged by weight (225-275g), were purchased from Charles River Laboratories (Wilmington, MA).
Wild animals	This study does not involve wild animals.
Field-collected samples	This study does not involve field-collected samples.
Ethics oversight	Both ex vivo and in vivo animal procedures were reviewed and approved by the Massachusetts Institute of Technology Committee on Animal Care (CAC).

Note that full information on the approval of the study protocol must also be provided in the manuscript.

Supplementary information

Dry double-sided tape for adhesion of wet tissues and devices

In the format provided by the
authors and unedited

Hyunwoo Yuk, Claudia E. Varela, Christoph S. Nabzdyk, Xinyu Mao, Robert F. Padera, Ellen T. Roche & Xuanhe Zhao

SUPPLEMENTARY INFORMATION

Dry Double-sided Tape for Adhesion of Wet Tissues and Devices

Hyunwoo Yuk, Claudia E. Varela, Christoph S. Nabzdyk, Xinyu Mao, Robert F. Padera,
Ellen T. Roche, Xuanhe Zhao*

*Correspondence and requests for materials should be addressed to X.Z. (zhaox@mit.edu)

This PDF file includes:

Supplementary Texts
Supplementary Figs. 1 to 16
Supplementary References

Other Supplementary Materials for this manuscript include the following:

Supplementary Videos 1 to 9

Surgical procedures and *in vivo* data analysis

All animal surgeries were reviewed and approved by the Committee on Animal Care at the Massachusetts Institute of Technology. Female Sprague Dawley rats (225-250 g, Charles River Laboratories) were used for all *in vivo* studies.

DST adhesion validation *in vivo*. Prior to the surgical procedure, gelatin-based DST (20 μm thickness) and thermoplastic polyurethane (TPU) films (75 μm thickness) were cut into circular patches by using a 5-mm-diameter sterile biopsy punch (Dynarex). The TPU films were functionalized with primary amine following the procedure described in Methods. All samples were prepared using sterile techniques and were further sterilized under UV light for 3 h.

For patch implantation, rats were anaesthetized using isoflurane (1–3% isoflurane in oxygen) in an anesthetizing chamber. Chest hair was removed. In addition to the pre-operative analgesic slow-release buprenorphine (1 mg kg⁻¹) administered subcutaneously, the regional nerve blocker lidocaine/bupivacaine was injected at the surgical site. Endotracheal intubation was performed and the animals were connected to a mechanical ventilator (Model 683, Harvard Apparatus) and placed over a heating pad for the duration of the surgery. A thoracotomy was performed in the third or fourth left intercostal space. The heart was exposed and the pericardium was removed using fine forceps. Either a DST-TPU hybrid patch ($n = 3$) or a TPU patch ($n = 3$) was placed onto the left ventricular epicardial surface (Supplementary Fig. 15a). To achieve adhesion of the DST-TPU hybrid patch, the surgeon positioned the DST and TPU layers on top of the epicardial surface on the left ventricle and gently pressed using forceps for 5 s. Adhesion was confirmed by pulling the edge of the patch and observing movement of the entire heart. To implant the TPU patch, 2 sutures (7-0 Prolene, Ethicon) were placed at opposite sides of the patch. Following the patch placement, the thoracotomy was closed using interrupted sutures (4-0 Vicryl, Ethicon) and 3-6 ml of saline was administered subcutaneously. The animal was ventilated with 100 % oxygen until autonomous breathing was regained, and the intubation catheter was removed. At 3 days following the patch implantation, the animals were euthanized by CO₂ inhalation. The hearts were excised and fixed in 10 % formalin for 24 h for histological analyses.

DST biocompatibility and biodegradability evaluation *in vivo*. Prior to implantation, 15 mm \times 10 mm rectangular gelatin-based DST samples (20 μm thickness) and chitosan-based DST samples (20 μm thickness) were prepared using sterile techniques and were further sterilized for 3 h under UV light.

For implantation in the dorsal subcutaneous space, rats were anaesthetized using isoflurane (1–2% isoflurane in oxygen) in an anesthetizing chamber. Anesthesia was maintained using a nose cone. Back hair was removed and the animals were placed over a heating pad for the duration of the surgery. The subcutaneous space was accessed by a 1-2 cm skin incision per implant in the center of the animal's back (Supplementary Fig. 15b). To create space for implant placement, blunt dissection was performed from the incision towards the animal shoulder blades. Either a rectangular DST sample ($n = 6$, gelatin-based; $n = 6$, chitosan-based) or a comparable volume of commercially-available tissue adhesive ($n = 4$, Coseal) was placed in the subcutaneous pocket created above the incision. The incision was closed using interrupted sutures (4-0 Vicryl, Ethicon) and 3-6 ml of saline were injected subcutaneously. Up to two implants were placed per animal ensuring no overlap between each subcutaneous pocket created. After 2 or 4 weeks following the implantation,

the animals were euthanized by CO₂ inhalation. Subcutaneous regions of interest were excised and fixed in 10 % formalin for 24 h for histological analyses.

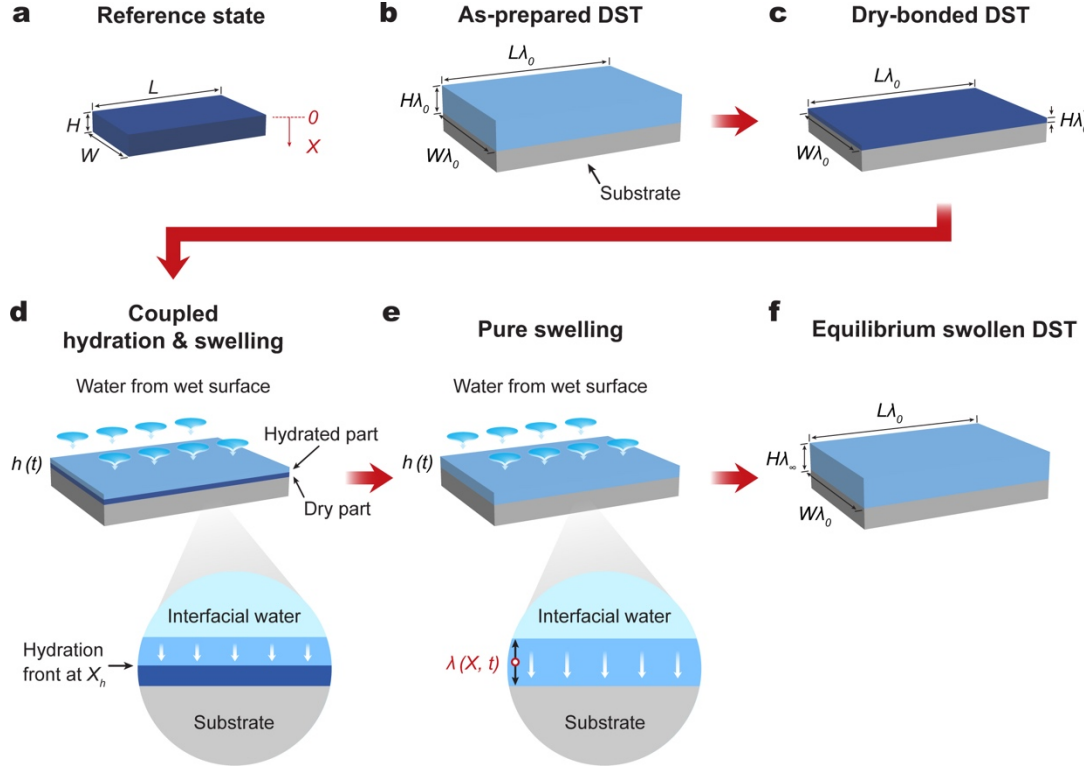
Histological processing. Fixed tissue samples were placed into 70 % ethanol and submitted for histological processing and hematoxylin and eosin (H&E) staining at the Hope Babette Tang (1983) Histology Facility in the Koch Institute for Integrative Cancer Research at the Massachusetts Institute of Technology. Histological assessment was performed by a blinded pathologist and representative images of each group were shown in the corresponding figures.

Quantitative model for drying interfacial water by the DST

To quantitatively understand the process of drying interfacial water by the DST in the dry-crosslinking mechanism, we develop a quantitative model for the hydration and swelling of the dry DST with experimental validation. Unlike wet hydrogels that exhibit pure swelling kinetics upon contact with wet surfaces, the dry DST first undergoes a coupled hydration and constrained swelling stage before transitioning into a pure constrained swelling stage. Supplementary Fig. 1 schematically illustrates the hydration and constrained swelling process of the dry DST. Upon contact with a wet surface, the initially dry DST (Supplementary Fig. 1c) absorbs interfacial water and advances a sharp hydration front within it, dividing the DST into a hydrated part and a dry part (Supplementary Fig. 1d). Meanwhile, the hydrated part of the DST swells as a wet hydrogel. Once the DST is fully hydrated, it can further swell by imbibing more water (Supplementary Fig. 1e) until it reaches the equilibrium swollen state (Supplementary Fig. 1f). Based on the abovementioned process, it is evident that:

- i) The total amount of interfacial water that a DST can absorb depends on the constrained swelling ratio of the DST.
- ii) The rate at which the interfacial water is absorbed by the DST depends on the kinetics of the coupled hydration and swelling and/or pure swelling of the DST.

In the following paragraphs, we will develop a quantitative physical model for water absorption by the DST, experimentally measure the physical parameters of the DST, experimentally validate the model, and provide a model-based prediction of the time required to absorb various amounts of interfacial water by the DST with different thicknesses.



Supplementary Fig. 1 | Hydration and constrained swelling process of the dry DST. **a**, A reference state for the DST in which the DST is fully dried and stress-free with length L , width W , and thickness H . The coordinate in the thickness direction X is defined from the upper surface of the DST where it will be exposed to the interfacial water. **b**, An as-prepared DST stretched by a ratio of λ_0 in all directions from the reference state. The as-prepared DST is bonded to a rigid substrate. **c**, The as-prepared DST is fully dried while bonded on the rigid substrate. Due to volume conservation, the thickness of the DST has been reduced by a ratio of λ_0^{-2} from the reference state. **d**, Upon contacting the wet surface, the dry DST first undergoes a coupled hydration and constrained swelling process. In this process, the interfacial water is absorbed by the dry DST and forms a sharp hydration front, which moves towards the substrate over time while the hydrated part of the DST further swells. **e**, When the dry DST is fully hydrated, it starts to undergo pure constrained swelling. **f**, In the equilibrium state, the swollen DST increases its thickness by a ratio of λ_∞ from the reference state.

1. Model for interfacial water absorption by the DST

We first define a reference state of the DST (Supplementary Fig. 1a) in which the DST is fully dried and stress-free, following the convention of previous models¹. The thickness, length and width of the DST at the reference state are denoted as H , L and W , respectively (Supplementary Fig. 1a). Due to the planar geometry of the DST, the hydration and swelling of the DST can be regarded as a one-dimensional process. In our model, we denote a point in the DST by its coordinate X along the thickness direction in the reference state (Supplementary Fig. 1a). It should be noted that the creasing instability can occur on the surface of the swollen DST if the swelling

ratio is above certain value^{2,3}. For simplicity of the analysis, we assume that the creasing instability does not significantly affect the water absorption process of the DST.

The first step to fabricate the DST is to make a hydrogel of the DST that swells from the reference state by a ratio of λ_0 along the thickness, length and width directions, and then bond the DST on a rigid substrate (Supplementary Fig. 1b). Thereafter, the DST is fully dried while maintaining constrained on the substrate. Compared to the reference state, the dry-bonded DST has been stretched by ratios of λ_0^{-2} , λ_0 and λ_0 along the thickness, length and width directions, respectively, due to volume conservation (Supplementary Fig. 1c). The dry-bonded DST is brought in contact with the wet surface at time $t = 0$, and subsequently the DST undergoes coupled hydration and swelling, (Supplementary Fig. 1d) and then pure swelling (Supplementary Fig. 1e), as discussed above. Due to constraint of the substrate, the DST can only swell along the thickness direction. The stretch ratio of a point along the thickness direction is denoted by $\lambda(X, t)$, which is a function of the coordinate X of the point and the time t in the process. The thickness of the DST in the current state is denoted by $h(t)$, which is a function of the time t in the process.

1.1. Equilibrium swelling of the DST

We first model the equilibrium swollen state of the DST (Supplementary Fig. 1f). At the equilibrium swollen state, the stretch ratio of the DST in the thickness direction is uniform, denoted as λ_∞ , and the stretch ratios in the length and width directions maintain to be λ_0 due to the constraint from the substrate (Supplementary Fig. 1f). For simplicity of the analysis, the swollen DST is taken as a Flory-Rehner hydrogel with thermodynamic parameters of N and χ , where N is the number of polymer chains per unit volume of the DST at the reference state (Supplementary Fig. 1a) and χ is the Flory solvent-polymer interaction parameter⁴. Therefore, the out-of-plane Cauchy stress σ in the swollen DST can be expressed as

$$\sigma = NkT \left(\lambda_\infty - \lambda_\infty^{-1} \right) \lambda_0^{-2} + \frac{kT}{v} \left[\log \left(1 - \lambda_\infty^{-1} \lambda_0^{-2} \right) + \lambda_\infty^{-1} \lambda_0^{-2} + \chi \lambda_\infty^{-2} \lambda_0^{-4} \right] \quad (\text{S1})$$

where k is the Boltzmann constant, T is the absolute temperature and v is the volume of a water molecule⁵. The first term of σ gives the stress due to stretching of polymer chains, and the second term gives the osmotic pressure due to mixing of polymer chains and water. Owing to the traction-free boundary condition, the out-of-plane Cauchy stress σ in the swollen DST is zero. Therefore, the equilibrium swelling ratio λ_∞ of the DST can be solved from Eq. S1, given that the thermodynamic parameters N and χ are known.

1.2. Kinetics for hydration of the dry DST

We find that the kinetics for hydration of the dry DST follows the Fickian-type moving-boundary theory. The position of the hydration front advances following a 1/2-power law with time⁶. Assuming that the dry DST begins to absorb water at time 0, the position of the hydration front X_h (defined in the reference state) in the DST at time t can be expressed as

$$X_h = K_h t^{1/2} \quad (\text{S2})$$

where K_h is defined as the hydration coefficient characterizing the hydration speed⁶⁻⁹. Therefore, the time to fully hydrate the dry DST with reference thickness H can be calculated as $\sqrt{H / K_h}$.

1.3. Kinetics of water transportation in the hydrated DST

Water transportation in the hydrated DST is found to follow the Fick's law^{1,5,9},

$$\frac{\partial \lambda}{\partial t} = D \frac{1}{\lambda_0^2} \frac{\partial}{\partial X} \left[\xi(\lambda) \frac{\partial \lambda}{\partial X} \right] \quad (S3)$$

where

$$\xi(\lambda) = \frac{1}{\lambda_0^2 \lambda^4} - \frac{2\chi(\lambda_0^2 \lambda - 1)}{\lambda_0^4 \lambda^5} + N\nu \frac{(\lambda_0^2 \lambda - 1)(\lambda^2 + 1)}{\lambda_0^2 \lambda^4} \quad (S4)$$

Since the top surface of the DST ($X = 0$) is in contact with interfacial water and reaches the equilibrium swollen state at time $t = 0$, we set the following boundary condition to solve Eqs. S3 and S4,

$$\lambda(X = 0, t \geq 0) = \lambda_\infty \quad (S5)$$

where λ_∞ can be solved from Eq. S1. When $0 \leq t \leq \sqrt{H / K_h}$, the DST undergoes coupled hydration and constrained swelling. The stretch ratio of the dry part is λ_0^{-2} (i.e., dry-bonded state), and the stretch ratio of the hydrated part can be solved from Eqs. S3-S5. When $t > \sqrt{H / K_h}$, the DST undergoes pure constrained swelling and the stretch of the hydrated DST can be solved from Eqs. S3-S5.

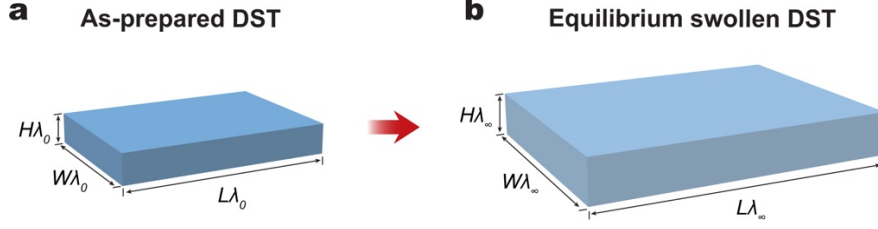
2. Measurement of physical parameters of the DST

2.1. Measurement of thermodynamic parameters of the DST

As discussed above, two thermodynamic parameters of the DST are involved during the swelling process, namely N and χ . To determine N , the shear modulus G_0 is measured for the as-prepared DST (Supplementary Fig. 2a) and N is then calculated from³

$$G_0 = \frac{1}{\lambda_0} N k T \quad (S6)$$

where λ_0 is measured by isotropically drying the as-prepared DST and taking the thickness ratio between the as-prepared state and the dry state.



Supplementary Fig. 2 | Free swelling of the as-prepared DST for measurement of χ . **a**, A freestanding as-prepared DST with a swelling ratio of λ_0 is submerged into a water bath. **b**, In the equilibrium state, the equilibrium swollen DST has a swelling ratio of λ_∞ in all dimensions.

Next, in order to measure χ , we carry out free-swelling experiments for the as-prepared DST without the constraint from the substrate (Supplementary Fig. 2a). The Cauchy stress σ in any direction of the unconstrained equilibrium swollen DST (Supplementary Fig. 2b) can be expressed as³

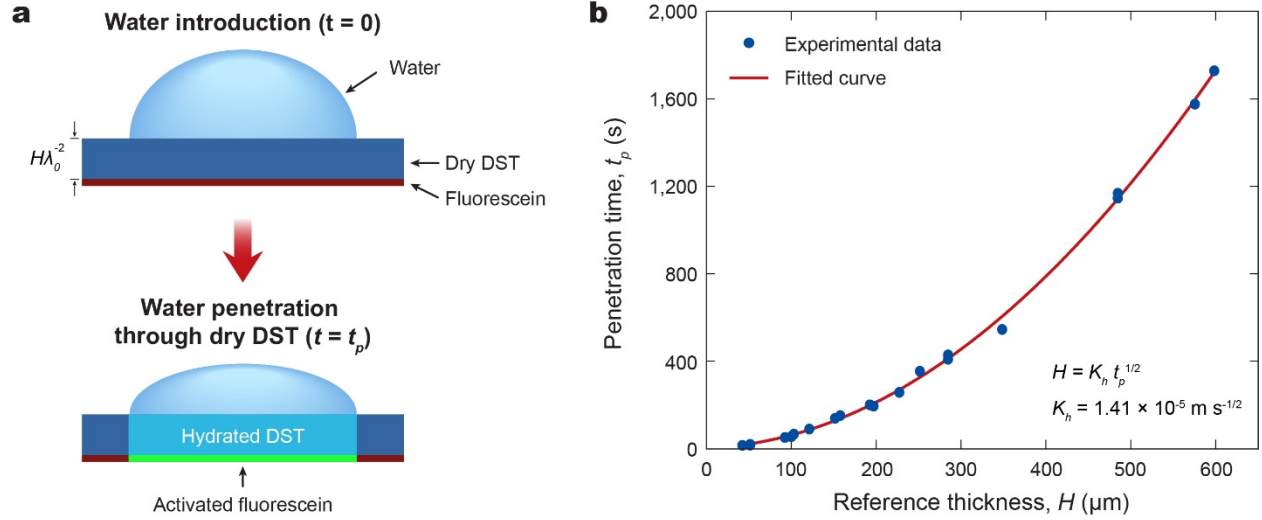
$$\sigma = NkT \left(\lambda_\infty^{-1} - \lambda_\infty^{-3} \right) + \frac{kT}{\nu} \left[\log(1 - \lambda_\infty^{-3}) + \lambda_\infty^{-3} + \chi \lambda_\infty^{-6} \right] \quad (\text{S7})$$

Due to the traction-free boundary condition, the Cauchy stress σ is zero in Eq. S7. Therefore, by measuring the equilibrium swelling ratio λ_∞ in Supplementary Fig. 2b, the parameter χ can be solved from Eq. S7. In this study, we use $T = 293$ K and $\nu = 3.0 \times 10^{-29} \text{ m}^3$. For the chitosan-based DST, the experimental measurements provide $G_0 = 11$ kPa, $\lambda_0 = 1.57$ and $\lambda_\infty/\lambda_0 = 2.42$, which yield $N = 4.27 \times 10^{24} \text{ m}^{-3}$ and $\chi = 0.41$.

2.2. Measurement of hydration parameter of the dry DST

The hydration kinetics of the dry DST is characterized by the hydration coefficient K_h in Eq. S2. To measure K_h , we record the time t_p to reach full hydration of the dry chitosan-based DST with varying reference thicknesses H (Supplementary Fig. 3). The hydration coefficient K_h can be fitted from the relation $H = K_h t_p^{1/2}$ based on Eq. S2.

As illustrated in Supplementary Fig. 3a, a layer of dry fluorescein is introduced to the bottom surface of the dry DST (with a thickness of $H\lambda_0^{-2}$) as a hydration indicator, since the fluorescein exhibits fluorescence only in the hydrated state. At $t = 0$, water is applied to the top surface of the dry DST. As the dry DST is fully hydrated and the bottom fluorescein layer starts to be activated, the penetration time t_p is recorded by observing the appearance of green fluorescence using a digital microscope (Dino Lite). By repeating the experiments for dry DST with varying reference thicknesses, a fitted penetration coefficient K_h of $1.41 \times 10^{-5} \text{ m s}^{-1/2}$ is obtained for the chitosan-based DST (Supplementary Fig. 3b).

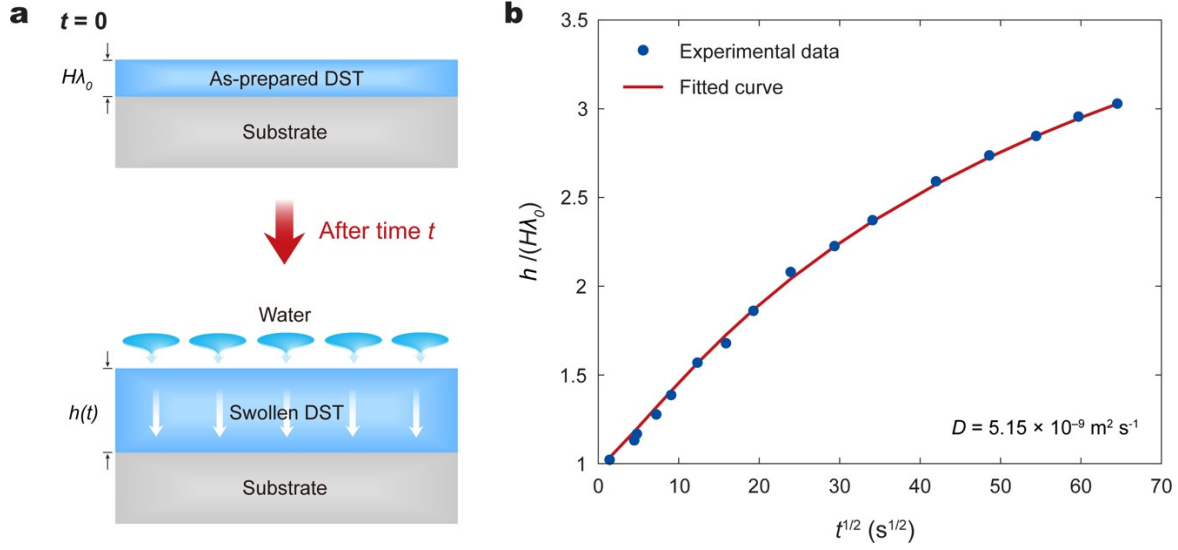


Supplementary Fig. 3 | Measurement of the hydration coefficient K_h of dry DST. **a**, Measurement setup for the penetration time t_p of a dry DST with thickness $H\lambda_0^{-2}$. A layer of fluorescein at the bottom surface of the dry DST serves as a hydration indicator. **b**, The measured penetration time t_p vs. reference thickness H . A fitted penetration coefficient K_h is $1.41 \times 10^{-5} \text{ m s}^{-1/2}$ based on the experimental data for the dry chitosan-based DST.

2.3. Measurement of water diffusivity in the hydrated DST

The diffusion kinetics of water in the hydrated DST is characterized by the diffusivity D in Eq. S3. To measure D , we carry out swelling tests using the chitosan-based as-prepared DST bonded on the glass substrate (Supplementary Fig. 4a). The as-prepared DST has a thickness of $H\lambda_0$. At time $t = 0$, the DST is soaked in water to swell, and the thickness of the DST h is recorded as a function of time t (Supplementary Fig. 4a).

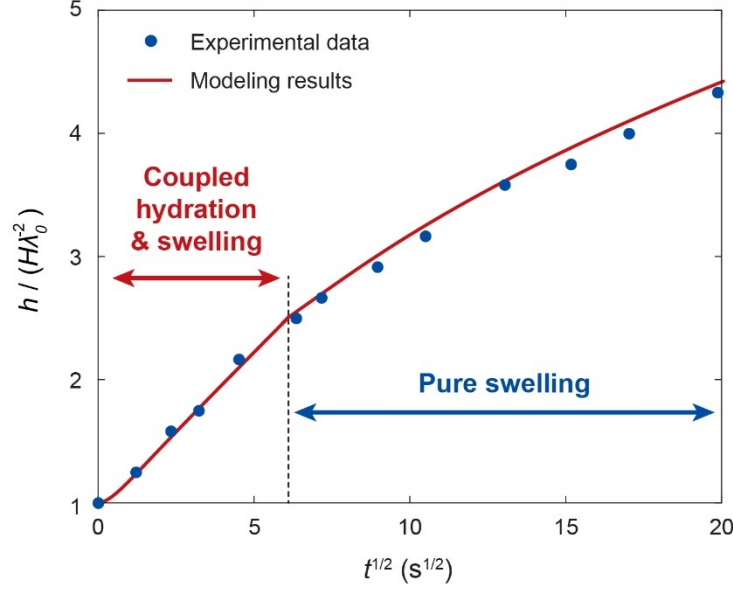
Since the thermodynamic parameters N and χ for the chitosan-based DST have been measured in Section 2.1., the relation between the thickness of the DST and time can be solved from Eqs. S3-S5 with a specific value of diffusivity D . Therefore, the diffusivity D for chitosan-based DST has been fitted to be $5.15 \times 10^{-9} \text{ m}^2 \text{ s}^{-1}$ from the experimentally measured thickness of the DST as a function of time (Supplementary Fig. 4b).



Supplementary Fig. 4 | Measurement of the diffusivity D of as-prepared DST. **a**, An as-prepared DST with an initial thickness of $H\lambda_0$ is bonded to a substrate. At $t = 0$, the DST starts to undergo constrained swelling process and the thickness h of the DST is recorded as a function of time. **b**, Normalized thickness $h/(H\lambda_0)$ vs. square root of time $t^{1/2}$ are experimentally obtained for the chitosan-based DST with an initial thickness $H\lambda_0$ of 135 μm . A diffusivity D is fitted to be $5.15 \times 10^{-9} \text{ m}^2 \text{ s}^{-1}$ based on the experimental data.

3. Experimental validation of the model

Next, we experimentally validate the model developed in *Section 1* based on the parameters measured in *Section 2*. We soak a dry-bonded chitosan-based DST (Supplementary Fig. 1c) in water at time $t = 0$, and then measure its thickness h as a function of time t . The experimentally measured and predicted relations between the thickness and time are compared in Supplementary Fig. 5. From the comparison, it is evident that the model with experimentally measured parameters can accurately predict the hydration and swelling process of the DST. In addition, the model can also differentiate the coupled hydration and swelling stage and the pure swelling stage of the DST (Supplementary Fig. 5).

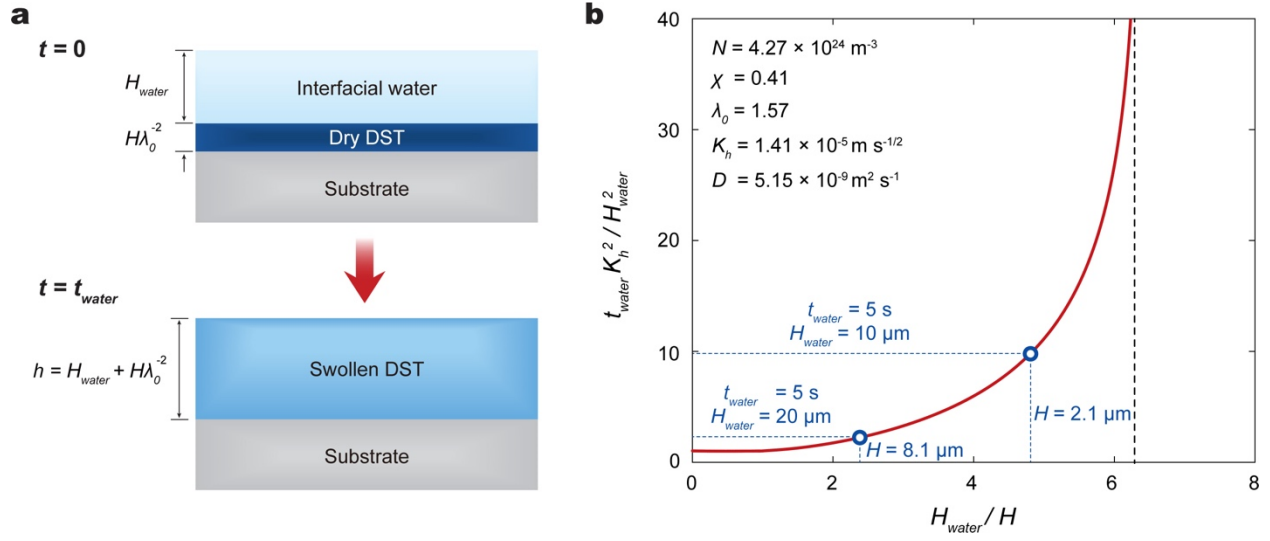


Supplementary Fig. 5 | Experimental validation of the model. Experimental and modeling relations between the normalized thickness of the DST $h / (H\lambda_0^{-2})$ vs. square root of time $t^{1/2}$ for coupled hydration and swelling and subsequent pure swelling of the dry DST. The dry DST has an initial thickness $H\lambda_0^{-2}$ of 56 μm .

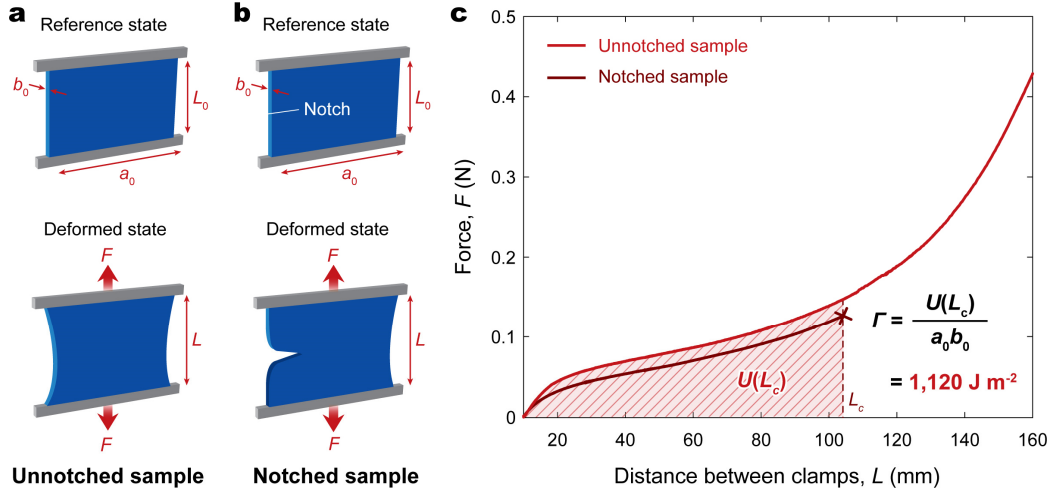
4. Prediction of time required to absorb interfacial water

Next, we aim to predict the time required to absorb different amounts of interfacial water by the DST with different thicknesses based on the developed model. At time $t = 0$, the dry DST with a thickness of $H\lambda_0^{-2}$ contacts a layer of interfacial water with thickness of H_{water} , and subsequently undergoes hydration and swelling processes. At $t = t_{\text{water}}$, the interfacial water is completely absorbed by the DST and the swollen DST has a final thickness of $h = H_{\text{water}} + H\lambda_0^{-2}$ (Supplementary Fig. 6a).

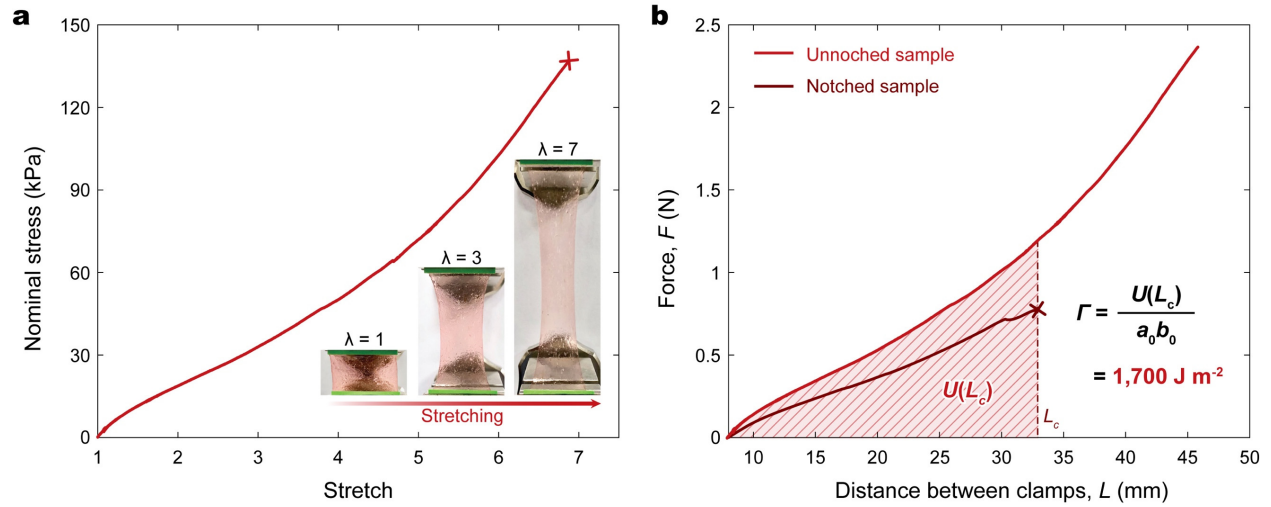
By solving Eqs. S2-S5 with the measured parameters in *Section 2*, we can calculate the time t_{water} required to absorb different amounts of interfacial water H_{water} by the DST with different reference thicknesses H . In Supplementary Fig. 6a, we present this relation with the normalized absorption time $t_{\text{water}} K_h^2 / H_{\text{water}}^2$ as a function of the normalized water thickness H_{water} / H . Since the fully swollen thickness of the DST is $H\lambda_\infty$, the maximum amount of water that can be absorbed by the DST is bounded by $H_{\text{water}} / H \leq \lambda_\infty - \lambda_0^{-2}$. When H_{water} / H exceeds $\lambda_\infty - \lambda_0^{-2}$, the DST cannot fully absorb the interfacial water. When H_{water} / H is below $\lambda_\infty - \lambda_0^{-2}$, it takes certain time to fully absorb the interfacial water according to Supplementary Fig. 6b. For example, if the DST needs to fully absorb 10 μm interfacial water layer within 5 s, the reference thickness of the DST should be over 2.1 μm . If the DST needs to fully absorb 20 μm interfacial water layer within 5 s, the reference thickness of the DST should be over 8.1 μm .



Supplementary Fig. 6 | Prediction of time required to absorb interfacial water by the dry DST. **a**, A schematic illustration of drying interfacial water by the dry DST. At $t = 0$, the dry DST with a thickness of $H\lambda_0^{-2}$ is in contact with an interfacial water layer with a thickness of H_{water} . At $t = t_{\text{water}}$, the interfacial water is completely absorbed by the DST, and the final thickness of the swollen DST is $H_{\text{water}} + H\lambda_0^{-2}$. **b**, Normalized time required to absorb interfacial water $t_{\text{water}}K_h^2/H_{\text{water}}^2$ vs. normalized thickness of water layer H_{water}/H for the chitosan-based DST ($K_h^2/D = 0.039$).

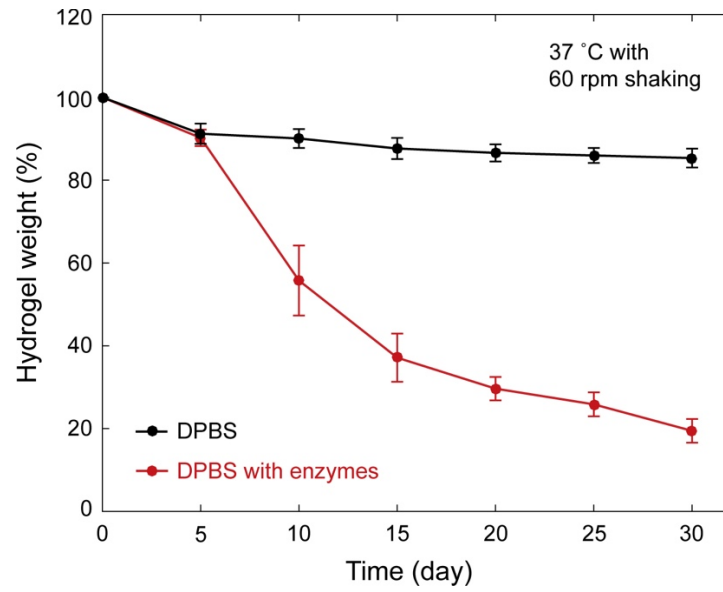


Supplementary Fig. 7 | Fracture toughness of the gelatin-based DST in the swollen state. a,b, Schematic illustrations of pure-shear test for an unnotched sample (a) and a notched sample (b). **c,** Force vs. distance between clamps for the unnotched and notched gelatin-based DST for fracture toughness measurement. L_c indicates the critical distance between the clamps at which the notch turns into a running crack. The measured fracture toughness of the gelatin-based DST is $1,120 \text{ J m}^{-2}$.

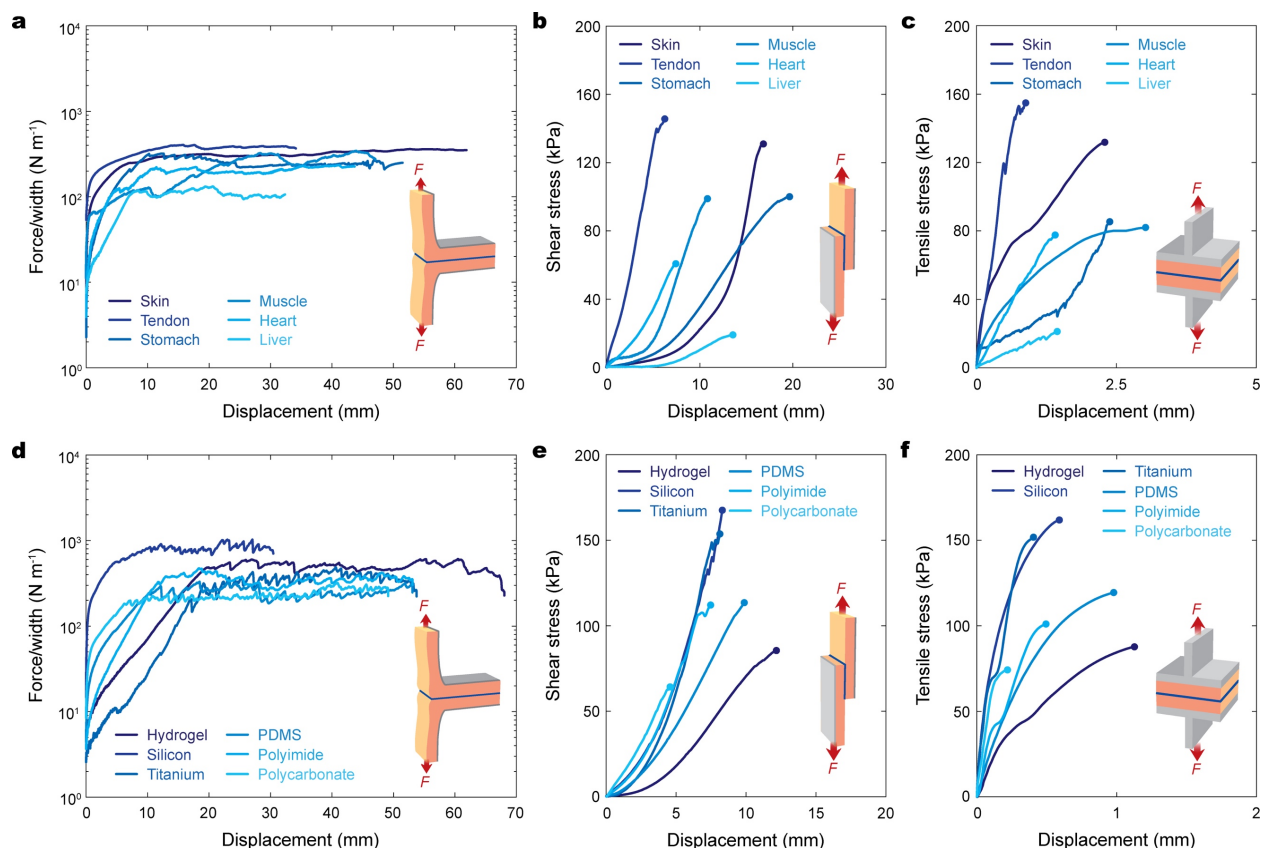


Supplementary Fig. 8 | Mechanical properties of the chitosan-based DST in the swollen state.

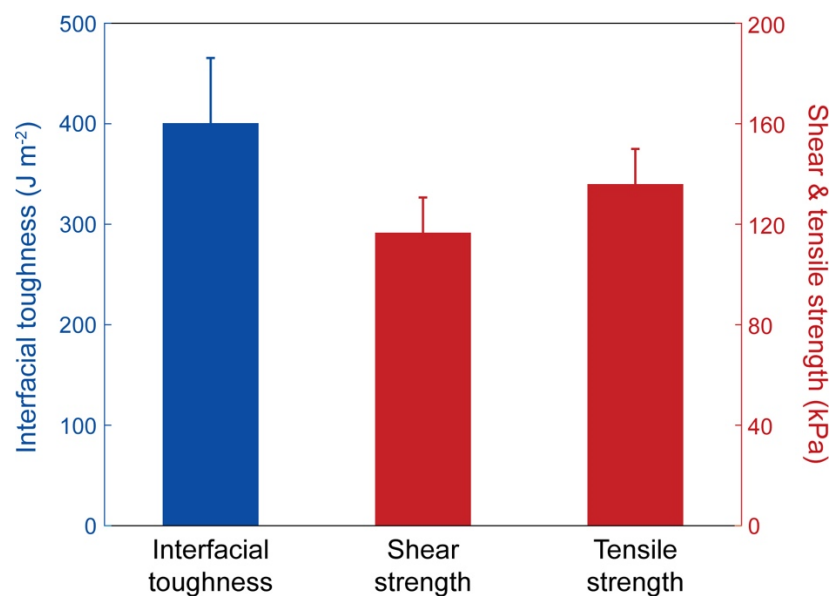
a, Nominal stress vs. stretch curve for the swollen chitosan-based DST. **b**, Force vs. distance between clamps for the unnotched and notched chitosan-based DST for fracture toughness measurement. L_c indicates the critical distance between the clamps at which the notch turns into a running crack. The fracture toughness is measured by using the method illustrated in Figure S7a, b. The measured fracture toughness of the chitosan-based DST is $1,700 \text{ J m}^{-2}$.



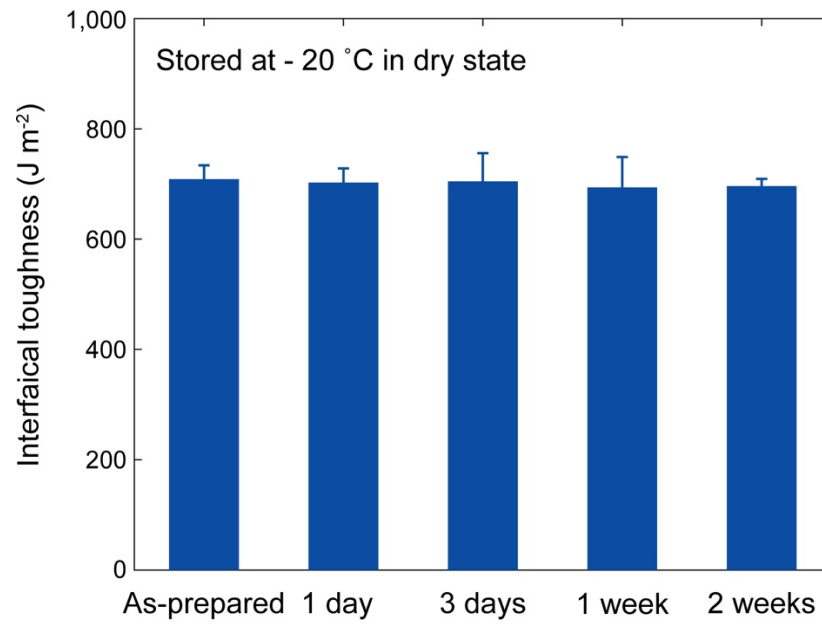
Supplementary Fig. 9 | *In vitro* biodegradation of the chitosan-based DST in DPBS with collagenase, lysozyme, and NAGase. Values represent the mean and the standard deviation ($n = 3-5$).



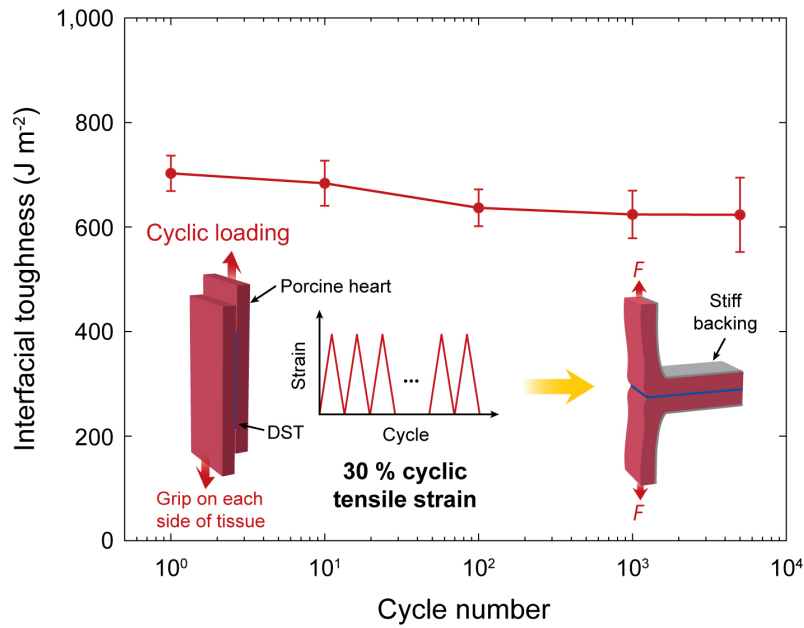
Supplementary Fig. 10 | Representative curves for mechanical tests of various tissues and engineering solids adhered by the DST. **a**, Force/width vs. displacement curves for 180-degree peeling tests of various tissues adhered by the DST. **b**, Shear stress vs. displacement curves for lap-shear tests of various tissues adhered by the DST. **c**, Tensile stress vs. displacement curves for tensile tests of various tissues adhered by the DST. **d**, Force/width vs. displacement curves for 180-degree peeling tests and 90-degree peeling tests (for silicon) of porcine skin and various engineering solids adhered by the DST. **e**, Shear stress vs. displacement curves for lap-shear tests of porcine skin and various engineering solids adhered by the DST. **f**, Tensile stress vs. displacement curves for tensile tests of porcine skin and various engineering solids adhered by the DST.



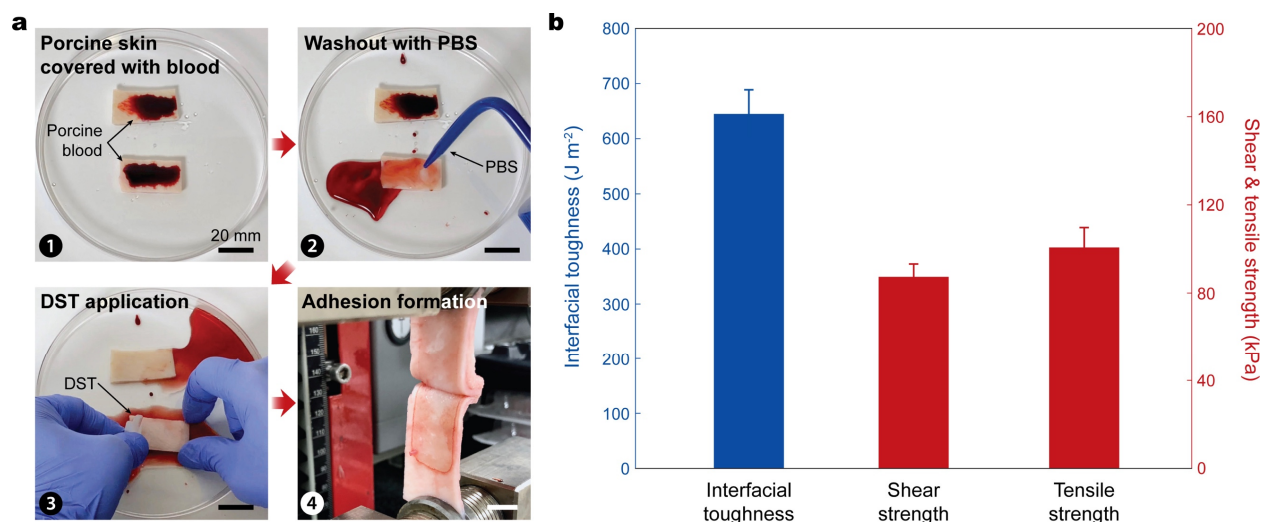
Supplementary Fig. 11 | Adhesion performance of the chitosan-based DST. Interfacial toughness, and shear and tensile strength between wet porcine skins adhered by the chitosan-based DST. All samples were kept in wet environments before the mechanical tests. Values represent the mean and the standard deviation ($n = 3-5$).



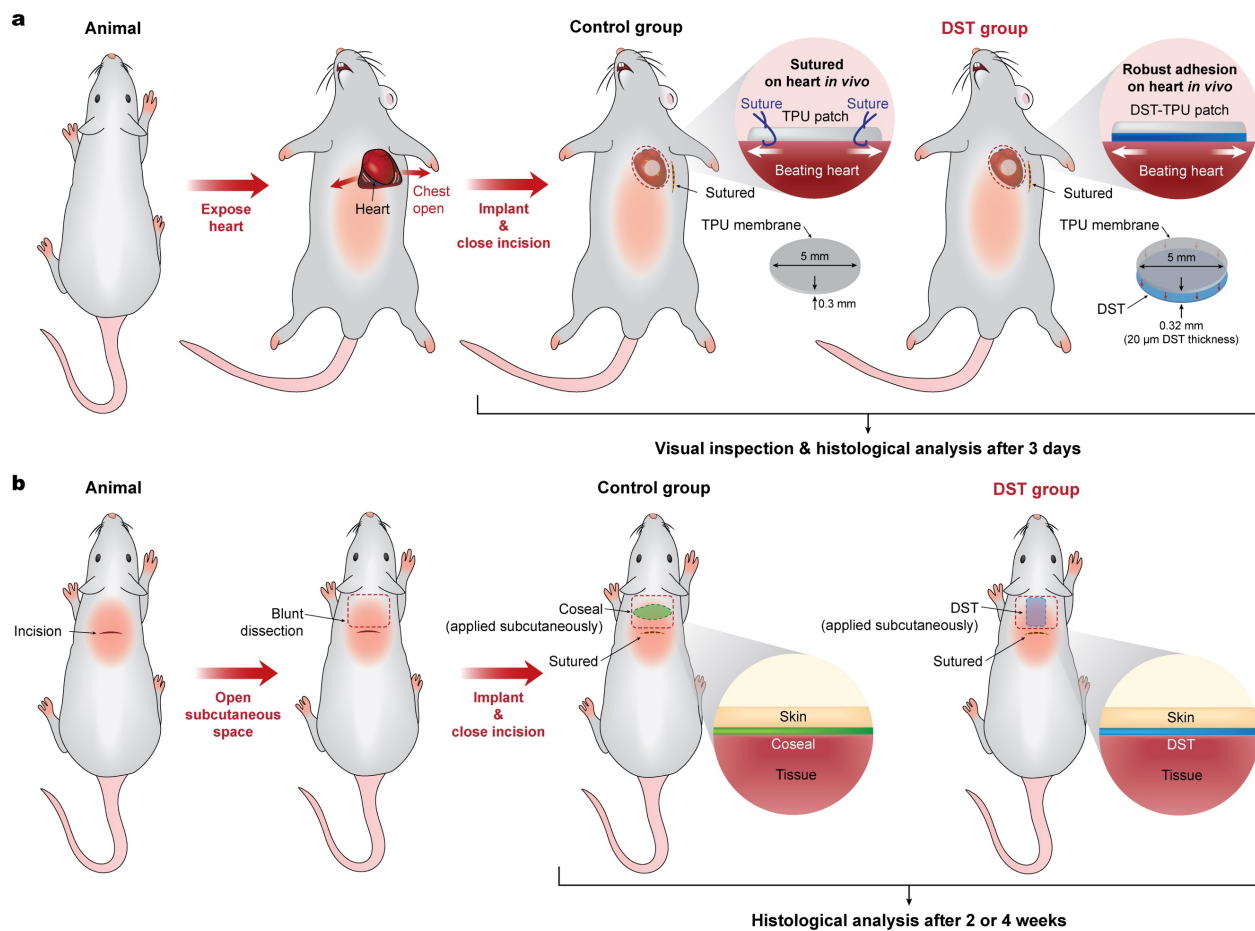
Supplementary Fig. 12 | Adhesion performance of the DST after storage. Interfacial toughness between wet porcine skins adhered by the DST stored at – 20 °C in the dry state for varying periods of time. Values represent the mean and the standard deviation ($n = 3-5$).



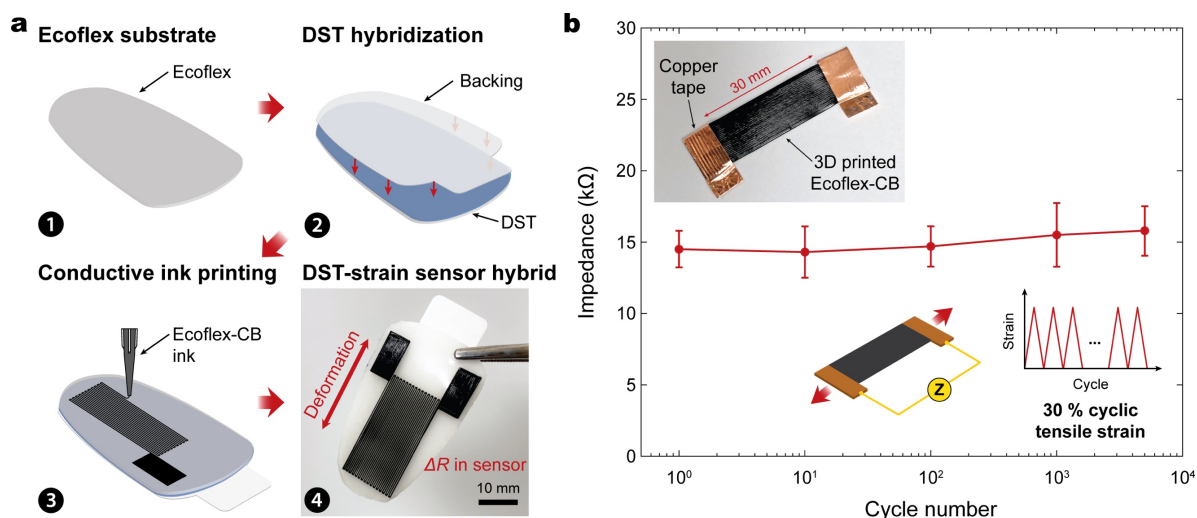
Supplementary Fig. 13 | Adhesion performance of the DST under cyclic loading. Interfacial toughness between two adhered porcine heart tissues by the DST as a function of the cyclic number of 30% tensile strain applied to the adhered tissues. All samples were kept in wet environments during the cyclic loading. Values represent the mean and the standard deviation ($n = 3-5$).



Supplementary Fig. 14 | Adhesion performance of the DST on tissues with blood. **a**, Adhesion between porcine skins with blood by the DST. **b**, Interfacial toughness and shear and tensile strength between porcine skins with blood adhered by the DST. All samples were kept in wet environments before the mechanical tests. Values in panel **b** represent the mean and the standard deviation ($n = 3-5$).



Supplementary Fig. 15 | Schematic illustrations for *in vivo* tests. a,b, Schematic illustrations for *in vivo* adhesion tests on rat heart (a) and biocompatibility and biodegradability implants in the rat dorsal subcutaneous pocket (b).



Supplementary Fig. 16 | Fabrication and cyclic stability of the DST-strain sensor hybrid. **a**, To prepare the DST-strain sensor hybrid, a DST-Ecoflex hybrid substrate was first prepared by using a hydrogel-elastomer hybridization technique¹⁰. A strain sensor was then fabricated by printing a conductive ink based on EcoflexTM resin and carbon black (CB). The resultant DST-strain sensor hybrid can be readily adhered onto wet tissues and measure deformations by monitoring changes in the electrical resistance of the strain sensor. **b**, Impedance of the printed Ecoflex-CB sensor as a function of the cyclic number of 30% tensile strain applied to the sensor. The printed Ecoflex-CB sensor exhibits stable impedance over thousands of cycles. Values in panel **b** represent the mean and the standard deviation ($n = 3-5$).

Supplementary References

- 1 Hong, W., Zhao, X., Zhou, J. & Suo, Z. A theory of coupled diffusion and large deformation in polymeric gels. *Journal of the Mechanics and Physics of Solids* **56**, 1779-1793 (2008).
- 2 Hohlfeld, E. & Mahadevan, L. Scale and nature of sulcification patterns. *Physical Review Letters* **109**, 025701 (2012).
- 3 Hong, W., Zhao, X. & Suo, Z. Formation of creases on the surfaces of elastomers and gels. *Applied Physics Letters* **95**, 111901 (2009).
- 4 Flory, P. J. *Principles of polymer chemistry*. (Cornell University Press, 1953).
- 5 Bouklas, N. & Huang, R. Swelling kinetics of polymer gels: comparison of linear and nonlinear theories. *Soft Matter* **8**, 8194-8203 (2012).
- 6 Crank, J. *The mathematics of diffusion*. (Oxford university press, 1979).
- 7 Crank, J. A theoretical investigation of the influence of molecular relaxation and internal stress on diffusion in polymers. *Journal of Polymer Science* **11**, 151-168 (1953).
- 8 Windle, A. in *Polymer Permeability* 75-118 (Springer, 1985).
- 9 Yoon, J., Cai, S., Suo, Z. & Hayward, R. C. Poroelastic swelling kinetics of thin hydrogel layers: comparison of theory and experiment. *Soft Matter* **6**, 6004-6012 (2010).
- 10 Yuk, H., Zhang, T., Parada, G. A., Liu, X. & Zhao, X. Skin-inspired hydrogel–elastomer hybrids with robust interfaces and functional microstructures. *Nature Communications* **7**, 12028 (2016).